7-11-2012

Computational and Experimental Studies of Catalytic Decomposition of H2O2 Monopropellant in MEMS-based Micropropulsion Systems

Stephen Widdis
University of Vermont

COMPUTATIONAL AND EXPERIMENTAL STUDIES OF CATALYTIC DECOMPOSITION OF H_2O_2 MONOPROPELLANT IN MEMS-BASED MICROPROPULSION SYSTEMS

A Thesis Presented

by

Stephen J. Widdis

to

The Faculty of the Graduate College

of

The University of Vermont

In Partial Fullfillment of the Requirements
for the Degree of Master of Science
Specializing in Mechanical Engineering

May, 2012

Abstract

The next generation of miniaturized satellites ("nanosats") feature dramatically reduced thrust and impulse requirements for purposes of spacecraft attitude control and maneuvering. Efforts at the University of Vermont have concentrated on developing a MEMS-based chemical micropropulsion system based on a rocket grade hydrogen peroxide (HTP) monopropellant fuel. A key component in the micropropulsion system is the catalytic reactor whose role is to chemically decompose the monopropellant, thereby releasing the fuel's chemical energy for thrust production. The present study is a joint computational and experimental design effort at developing a MEMS-based micro-reactor for incorporation into a monopropellant micropropulsion system. Numerically, 0D and simplified 2D models have been developed to validate the model and characterize heat and mass diffusion in the channel. This model will then be extended to a 2D model including all geometric complexities of the catalyst bed geometry with the goal of optimization. Experimentally, both meso and micro scale catalyst geometries have been constructed to prove the feasibility of using RuO_2 nanostructures as an in situ in a microchannel.

Acknowledgements

First, and foremost, I would like to thank Professor Darren Hitt, whose support, guidance and patience made this work possible.

I would also like the thank Dr. Walter Varhue, Dr. Michael Cross, and Kofi Asnte for their contributions.

Funding for this work has been provided by NASA under Cooperative Agreement #NNX09A09.

To my dear friend Ryan Hawks, whose life and legacy serve to encourage me to never settle for less than my dreams while always accomplishing my goals. You will never cease to inspire me.

Peace, Love and Deep Powder.

11/13/1985-3/1/2011

Table of Contents

List of Tables

List of Figures

Chapter 1

Introduction

As microelectricalmechanical system (MEMS) technologies progress, NASA and the AFOSR have shown growing interest in designing the next generation of spacecraft. "Nanosats", or sub 10 kg autonomous satellites capable of operating in distributed networks ("formation flying") and performing mission objectives not currently achievable with traditional satellite architectures, are a good example of the next generation of solutions sought by NASA. Their reduced mass cuts launch costs which can account for 30% of total mission cost. A network of several small spacecrafts can also reduce mission risk as loss of a single device would not end an entire mission. Thus far nanosats have been passive spacecraft with the first devices dating back to the Explorer program in the mid 1960s. In 2000 launch devices capable of deploying several nanosats simultaneously led to the creation of the CubeSat program by Stanford and California Polytechnic State University. The CubeSat program established dimensional, mass, and electrical standards to reduce launch costs. CubeSats are 10 cm cubes with some variations as large as 12.5 x 12.5 x 25 cm.[13] Currently deployed CubeSats are passive and lack the ability to perform attitude control, station keeping, or orbital maneuvers, which will be critical to further missions. While nanosats will

require micro-scale propulsion because of their small size, larger satellites in development also need micro-level thrust to meet mission goals. NASA's laser interferometry space antenna (LISA) is an example of a larger scale mission requiring high precision thrust generation to support formation flying. For this mission three separate 500kg satellites held at Lagrange points in a triangular formation separated by 5,000,000 km while maintaining tolerances of 30 nrad and 10 nm study gravitational waves. Figure 1.1 is a conceptual sketch provided by NASA. A maximum of $30\mu N$ will be provided by three clusters of four thrusters to facilitate drag free operation. In drag free operation the space craft flies around its test mass keeping the mass centered with a tolerance of only 10 nanometers. Test masses are 2 kg 46 mm cubes composed of gold and platinum. The exterior spacecraft blocks the test mass from external forces such as aerodynamic drag and solar pressure allowing the test mass to experience unperturbed flight and to determine the flight path.[2]

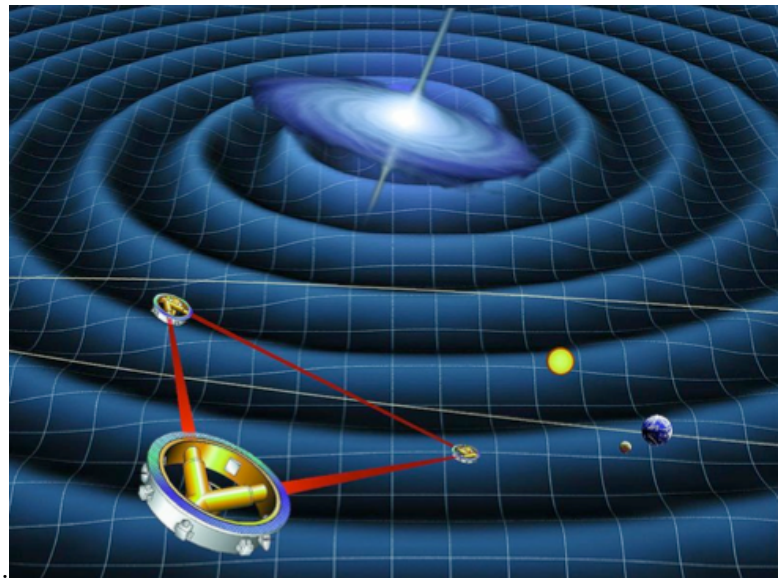

Figure 1.1: Laser Interferometry Space Antenna (LISA) is a recently cancelled NASA/ESA joint venture to study gravitational waves. This conceptual sketch of the three satellites flying in a triangular configuration, each separated by 5 million kilometers courtesy of NASA [2].

1.1 Micropropulsion

Due to their vastly reduced size, nanosats require propulsion technologies that can provide very low thrust, specific impulses, and impulse bits, while meeting size, mass, power and cost constraints associated with a small device. Many different thruster types have been explored for use on the micro scale; for a complete review see Mueller[19]. Different monopropellants have been used for propulsion and attitude control for decades and are much simpler than bipropellants while offering impulse control not afforded by solid rockets. Figure 1.2 is a schematic representation of the operation of a monopropellant thruster.

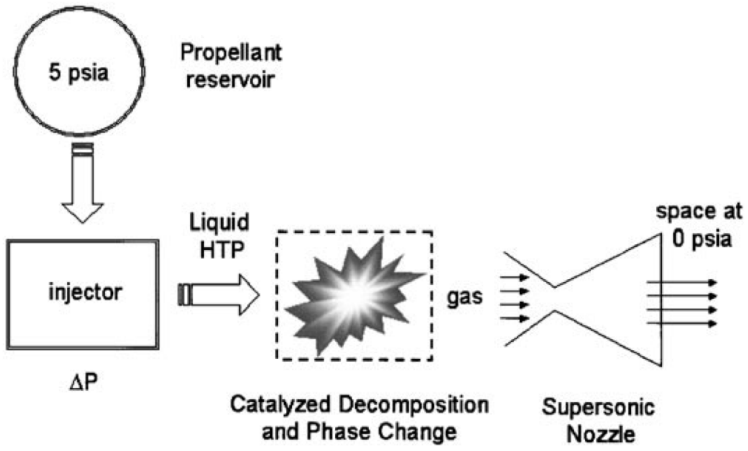

Figure 1.2: This schematic representation of monopropellant thruster shows the key elements of a standard system. Fuel is held in a pressurized tank. The injector section facilitates flow from the holding tank to the catalytic chamber while dropping pressure slightly to prevent backflow. In the catalytic chamber the fuel is decomposed causing heating and subsequent fluid expansion. The hot gas is then fed into a supersonic nozzle that produces the desired thrust.

Rocket grade hydrogen peroxide (HTP) is a good fuel choice for this application because it is fairly stable and non-toxic as opposed to hydrazine. When hydrogen peroxide is exposed to a catalyst it decomposes exothermically into water and oxygen releasing 98 kJ/mol with an adiabatic flame temperature of 1220 K. Approximately

44 kJ/mol are used to vaporize the water resulting an an excess of 54 kJ/mol.

$$H_2O_2 \rightarrow H_2O + .5\ O_2 + Q \tag{1.1}$$

While pure H_2O_2 is not available commercially, 90% and 98% solutions are readily available for purchase from many suppliers, including FMC Corp. When the concentration is reduced the excess energy is reduced to 37.15 kJ/mol by the additional water content. In the past hydrogen peroxide has been passed over in favor of hydrazine due to storage and contamination issues with HTP. Data shows that with increased concentration oxygen loss decreases due to the reduced water content and therefore less ionization occurs. FMC has published data showing that with proper material selection 90% HTP decomposes less than 0.25% per year and 98% HTP oxygen loss is even lower at 0.07% per year. Increased surface tension reduces surface wetting and may play a factor in increased stability. When samples of 90% and 98% HTP were held at 100°C for 24 hours the former realized 2.57 times more oxygen than the later. The SynCom II communication satellite launched into geosynchronous orbit at 23,000 miles in 1963 held H_2O_2 in pressurized tanks. In the first year no noticeable decrease in specific impulse was observed.[16] 90% HTP offers a modest specific impulse ($I_{SP} = 150s$), but a relatively high storage density ($> 1300\frac{kg}{m^3}$).[24] While HTP has been proven as a monopropellant and as part of different bipropellants for decades, scaling previous designs for use at the micro-scale has proven difficult.

1.2 MEMS Catalysis

When hydrogen peroxide is decomposed to generate thrust a catalyst must be used to accelerate the rate of decomposition. All chemical reactions are governed by thermodynamics that determine whether a reaction will move forward and how far the

reaction will go. For some chemical reactions to move forward energy must be added to the system; this energy is termed the activation energy. A catalyst is a substance that increases the rate at which a chemical system reaches equilibrium by reducing the activation energy, without being consumed in the process.[3]. Figure 1.3 depicts the effect of a catalyst on a chemical reaction.

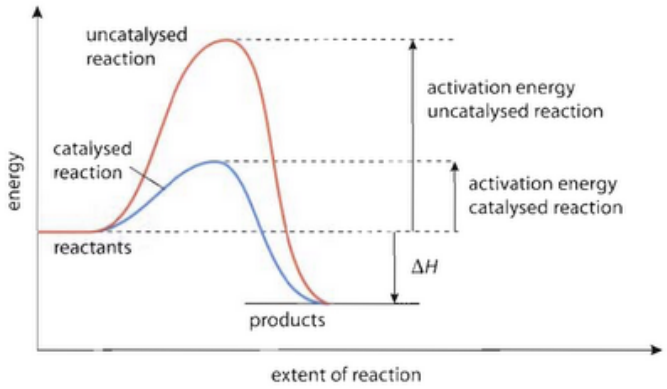

Figure 1.3: The introduction of a catalyst makes a reaction more likely to move forward by reducing the energy needed to initiate the reaction, called activation energy.

Catalysis can be either homogenous if the catalyst is of the same phase as the reacting flow, or heterogeneous if the catalyst is not of the same phase. Monopropellants utilize the later with a solid catalyst and a multiphase liquid/gas flow. In the past, a stack of silver coated steel screens were the primary catalyst. Cervone et al.[5] developed an HTP rocket providing thrust levels of 5 N using silver gauze and pellets as the catalyst. To achieve lower thrust levels, chamber widths on the order of 1000 μm are required and these techniques become inadequate.

In an October 2001 publication Hitt et al.[11] developed a MEMS-based solution for scaling thrust to a level commensurate with the needs of nanosats; the design criterion is shown in Table 1.1. The goal of this project was to produce 1-500 μN of force with a specific impulse of 140-180s for station keeping and precise orbital maneuvers. Several propulsion methods were discussed and a monopropellant hydrogen

peroxide method was chosen because of the high thrust-to-weight ratio chemical propellants can provide combined with the relative ease of handling of peroxide. Surface reactions are well suited for MEMs applications due to the intrinsically high surface to volume ratio. Hitt et al. concluded that traditional packed bed or screen configurations are not feasible on the micro-scale. With width and depth of the channel set from the design parameters, a length scale must be determined. Lack of sound understanding of catalysis in MEMS devices made estimates of the critical length needed for complete decomposition difficult to ascertain. An empirical approach of scaling macro scale lengths to MEMS devices based on empirical data from literature of larger HTP thrusters resulted in an estimated length of 1.7-2 mm. With these values fixed, different strategies for increasing surface area were considered. Fabrication concerns restricted the design to straight walls. Two prototype configurations were tested. The first design consisted of parallel zig-zag configurations as seen in Figure 1.4(a). The second was a chamber with an array of square pillars oriented at 45° to the flow and coated with silver via vapor deposition method. The pillars serve as a "micro packed bed" drastically increasing the surface area and decrease the free stream diameter of individual flows, as seen in Figure 1.4(b).[11] .

The fabrication process makes prototyping and testing difficult, but is well suited for mass production as several hundred can be etched on a single wafer and then separated. Thrusters were etched to varied depths into 500 μm thick silicon substrates using the deep reactive ion etching method (DRIE). This procedure provides high precision fabrication of very small features. Figure 1.5(a) is an SEM photo of the entire geometry. The scale in this figure is 2 mm. In Figure 1.5(b) pillars have been intentionally damaged after etching to allow for better inspection of the chamber. Here the high precision of the etch is evident proving the ability to maintain vertical uniformity for the etch depth of 100 μm. After applying a silver surface coating, a

Table 1.1: GSFC operating requirements as set forth by Hitt et al.[11] were taken as design constraints for this project.

Propulsion system parameter	Target value or range
Thrust level	1-500 μN
Impulse bit	1-100 μNs
Maximum specific impulse	1185 s
Mass flow rate	$400\mu g/s$
Throat area	$9000\mu m^2$
Inlet pressure	$5-6psia$
Outlet pressure	≈ 0 $psia$
Mass	< 0.1 kg
Power consumption	< 1 W
Volume	< 1 cm^3
Operating temperature	< 1700 K

Pyrex cover slide was anodically bonded to the substrate. Glass was chosen to allow for visual inspection, but could be replaced with silicon for production. The individual thrusters were then separated using a diamond saw. A photo of a completed NASA GSFC prototype has been included to provide a sense of scale (Figure 1.6(a)).

Both configurations successfully generated small gas bubbles that coalesced into larger bubbles. In the pillar configuration, large bubbles became lodged and choked portions of the flow. Target lengths of 2 mm were predicted empirically but experimentally lengths of 2.5 mm only achieved 85% decomposition. Figure 1.6(b) shows a largely liquid exhaust from the pillar prototype. At this scale the Reynolds number is very low leading to laminar flow regardless of the geometry and therefore very little mixing occurs. Thus diffusion and conduction are the sole modes of species and heat transport. If the flow width is too large, the center of the flow will be largely unaffected by the reaction at the surface. Related concerns motivated efforts to accurately predict the optimal chamber geometry for a range of expected flow conditions. The critical channel dimension (length) must be selected such that, for a given mass flow

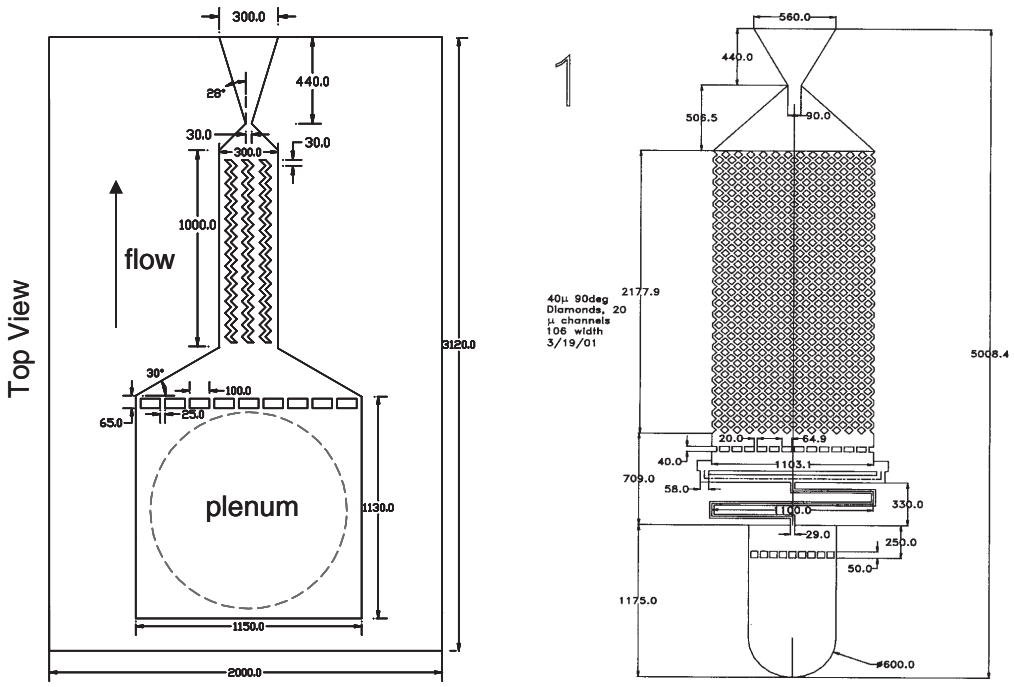

(a) (b)

Figure 1.4: Pictured are mechanical drawings showing the top views of the NASA Goddard thruster designs and shows their evolution. All dimensions are in microns. Etch depths varied from 100-300 μm (a) The original design consisted of a zig-zag pattern and lacked an injector section. (b) The more recent configuration included an array of pillars. From bottom to top the flow begins in the plenum and moves through pillars meant to act as a simple filter. Next the injector section serves to drop the pressure approximately 5 psia. to prevent back flow. Next an array of rectangular pillars align the flow. Then an array of square pillars with $40\mu m$ sides are oriented at 45° to the flow. The pillars are spaced 20 μm apart creating individual flows and inherent symmetry when sufficiently far from the channel boundaries. These individual flows will be studied rather than the system as a whole. [11]

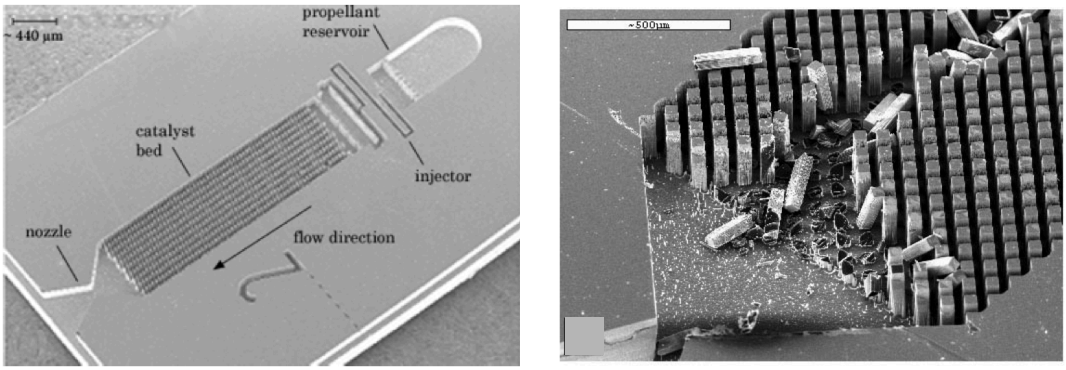

(a) (b)

Figure 1.5: SEM photography was used to capture images of the etched thruster. (a) The completed thruster with its individual parts labeled is shown first. (b) Here the pillars have been intentionally removed to reveal the surface below. [11]

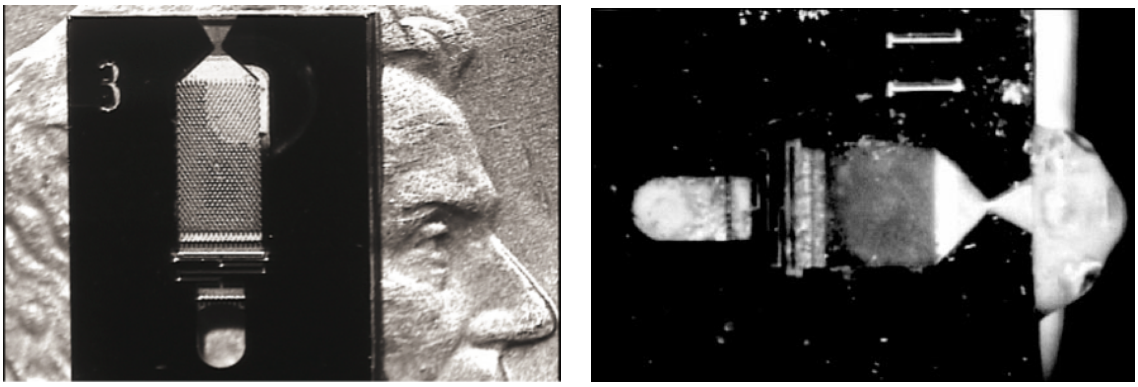

(a) (b)

Figure 1.6: (a)Pictured is a complete NASA GSFC thruster placed on a standard US penny to provide scale. (b) The second figure shows experimental results obtained by Hitt et al. after a run time of 13.5 s. The exit plume to the right of the image is highly energetic but contains a significant portion of water suggesting incomplete decomposition. A quantitative comparison favored the pillar configuration over the previous "zig-zag" design. [11]

rate, complete decomposition occurs. If the chamber is too short, incomplete decomposition will result in diminished efficiency. If the channel is too long condensation may occur; the consequences of which have been studied by Greenfield et al.[9].

John J. Rusek explored different catalysts and characterized their effectiveness in decomposing hydrogen peroxide.[21] Rusek describes that catalysis is limited by available catalytic surfaces and the quality of the surfaces. Analytical methods for the assay of HTP are discussed for adapting macro scale techniques to MEMS devices. Rusek tested oxides of silver, ruthenium, manganese, lead, vanadium, and chromium. Alumina spheres and cylinders were impregnated with catalyst by soaking for 4 hours. The spheres were then dried in an $80°C$ oven and cooled. Calcination was performed above metallic transition temperature for 15 hours. Base diameters ranged from 1/16 to 1/8 inch. Bases were weighed before and after impregnation to determine loading. To evaluate batch activity for each catalyst, a 50 ml spherical flask containing 20 ml of 70% peroxide was stirred continuously. A precise amount of catalyst was added at $t = 0$ and samples were removed at time intervals for measurement using refractometry. Results were plotted as $\ln(\frac{Ca}{Ca_0})$ vs. time. Here Ca is the time dependent concentration of hydrogen peroxide and Ca_0 is the initial batch concentration. Using the relationship $-\ln(\frac{Ca}{Ca_0}) = kt$, the first order rate constant was determined. This was then normalized by the catalytic metal loading in moles resulting in k'. These values were then normalized by the lead active catalyst to determined relative activity. The results from Rusek's study are listed in Table 1.2. Ruthenium oxide shows a very high relative activity compared to the other oxides tested. Rusek warns that the loading for this test was very low and the results should be viewed with caution. It should be noted, however, that the manganous species also show relative activities one order of magnitude greater than the industry standard, silver, which shows a rather low relative activity.

Table 1.2: Batch activity testing results for selected catalysts using 70 % FMC hydrogen peroxide recreated from work performed by Rusek et al.[21]

Catalyst	Impregnated loading, $wt\%$	Calcined loading, $wt\%$	k, $10^{-6}s^{-1}$	k', $s^{-1}mol^{-1}$	Relative activity
Ag_2O	1.10	1.18	19.3	0.580	1.5
RuO_2	0.04	0.01	4.18	15.5	41
MnO_2	7.27	0.14	19.4	5.67	15
MnO_3	7.27	0.33	38.0	4.45	12
K,Mn_xO_y	0.15	0.16	40.6	5.58	15
PbO	1.50	1.61	8.35	0.376	1
V_2O_5	0.42	0.40	8.3	0.485	1.3

RuO_2 is ideal for this application because it can be "grown" natively on the substrate forming a bond with the surface of the catalyst bed. Nanorods also serve to drastically increase surface area because they extend off the walls into the bulk flow. A nanorod is a nano catalyst defined as a material that acts as a chemical catalyst and whose physical size is between 10 and 1000 nm. On this scale unique physical and chemical properties can be exploited to enhance catalytic performance. Nanorods are self-assembled structures whose shapes are governed by the physical and chemical nature of the material. Due to their small size, nanorods provide a large surface-to-volume ratio, which is advantageous for promoting surface reactions. Nanorods are grown on silicon substrates using reactive radio frequency sputtering in an electron cyclotron resonant plasma process, the details of which can be found in work by Cross et al.[7]. Cross explains that by controlling reactor conditions and substrate temperature both nanorod density and length can be controlled. These square nanorods are approximately $1.5\mu m$ in length and range from approximately 25nm to 165nm across. They can be grown at densities of up to 15 per μm^2. Assuming a square cross section of $0.1\mu m$, length of $1\mu m$, and a density of 10 per μm^2 the available surface area is increased 14 fold when compared to a simple surface coating.

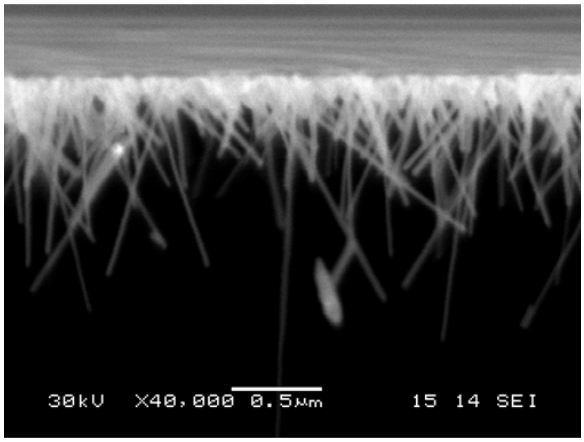

Figure 1.7: Cross et al. have grown ruthenium nano rods on silicon substrates with great uniformity in both length and density as seen in this image.

1.3 Computational Models

Several research groups around the world have attempted to computationally model the decomposition in different geometries in an effort to optimize devices for a wide range of applications. Bonifacio and Sorge used a lumped-parameter method to model heat and mass transfer in a monolithic channel to rapidly size reactors. The performance of the reactor was studied by parametrically varying design parameters such as flow rate, injection temperature, size, and shape. Bonifacio states that a full simulation of the "real decomposition process" is too complex and computationally costly to justify such an endeavor. Bonifacio cites the many phenomena involved such as diffusion and wall processes, as well as the interdependence of heat and mass transport as prohibiting factors. When constructing a reduced order model, processes with the greatest contribution to critical length must be identified. Temperature is found to rise slowly until the ignition temperature is reached. Determination of the location of the detention point is the main objective. To this end the model assumes the gas phase temperature, concentration, and velocity are constant across the cross section and axial conduction is ignored. Since the detention temperature is reached

after the solution has been completely vaporized, the initial condition for the model is a gaseous inlet at 423 K. Two models were considered: a circular cross section with 1mm diameter and a parallel plate configuration separated by 1 mm. Results showed that while the lumped parameter method accurately predicted the location of the detonation, it fell short of fully characterizing the flow.[4]. The European Space Agency(ESA) has invested heavily in the use of hydrogen peroxide as a monopropellant. As part of this effort the Green Advanced Space Propulsion project (GRASP) was established in December of 2008. As part of GRASP, Maricelti generated 2D and 3D models of a 6 mm diameter cylindrical chamber as well as honeycomb reactor using Arrhenius relations with an activation energy of 50.2 kJ and an exponential prefactor of $1.1 \times 10^8 s^{-1}$. This model consisted of adiabatic walls, a mass flow inlet, and a pressure outlet. Results for varied kinetic parameters as well as design parameters were compared[15] showing the precedent for modeling H_2O_2 decomposition in micro reactors.

Previous work at the University of Vermont has characterized the flow in an attempt to optimize the geometry by modeling the decomposition of 85% hydrogen peroxide. In a series of three publications, Zhou et al. computationally modeled catalysis of HTP. In the first paper, Zhou modeled a constant rate volumetric decomposition as a first pass at the high order surface reaction.[25] Here a steady one-dimensional model with a fixed reaction rate constant of $k = 10^8 s^{-1}$ in a simple microchannel was modeled resulting in decomposition lengths of 10-15 channel diameters under the required flow conditions. For a 10 μm wide channel this would equate to .1-.15 mm. Zhou breaks down the flow into 5 district regions as depicted in Figure 1.8. Region I consists of liquid phase peroxide and water, which is heated from $T_{initial}$ to $T_{sat}^{H_2O}$. In Region II the liquid water is vaporized. The mixture is then heated to $T_{sat}^{H_2O_2}$ in Region III. In Region IV liquid hydrogen peroxide is vaporized at a static tem-

perature ($T_{vap}^{H_2O_2}$) leaving a gaseous mixture at the beginning of Region V where the remainder of decomposition takes place. Zhou shows that the first 4 regions equate to a "preheating" and have a minimal contribution to critical length. Zhou goes on to suggest that while the first 4 regions can be modeled using thermodynamic equations of state, region V is more complex and cannot in general be solved in closed form. The idealized model with 100% hydrogen peroxide determined region I-IV to take only 6 μm with complete decomposition in 150 μm at a final temperature of 1162 K. Strong dependence on reaction rate, mass flux, and concentration were observed.

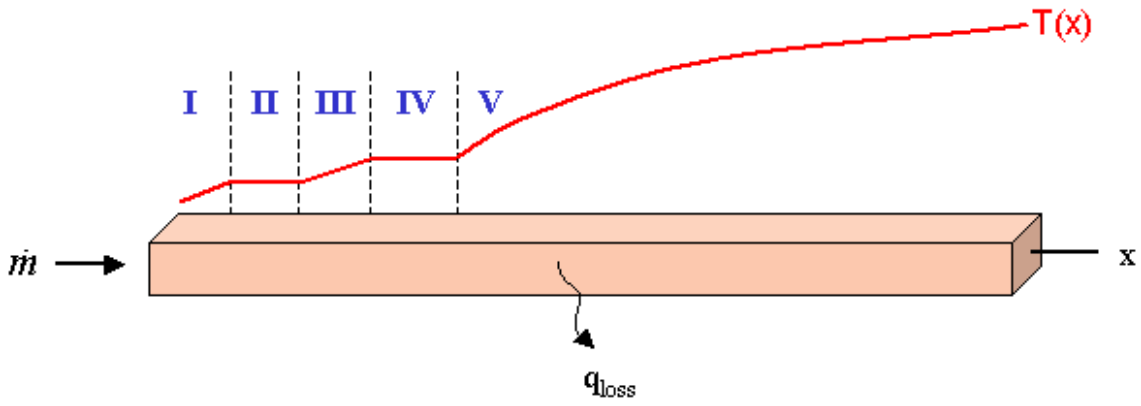

Figure 1.8: Representation of the 5 distinct flow regions. Images courtesy of Zhou[26]

In a later paper the Arrhenius equation was implemented in a steady one-dimensional model[26]. Here Zhou developed three dimensionless parameters to describe the flow: the Damköhler number(Da), the Zeldovich number(Ze), and the heat release parameter(C_e).

$$Da = \frac{\rho_0 \Lambda L}{G}, \quad Ze = \alpha \frac{T_A}{T_f}, \quad C_e = \frac{Y_0 Q}{c_P T_0} \tag{1.2}$$

The Damköhler number(Da) is the ratio of residence and chemical kinetic time scale, while the Zeldovich number is dimensionless activation energy, and the heat release parameter is a measure of stored energy based on inlet concentration. Matlab was

used to solve this two point boundary value algorithm. Pressure is held constant at atmospheric. Material properties were assumed constant in the first four regions. Region V utilized ideal gas laws to determine density. This model found that vaporization was completed in 186 μm with complete decomposition in 1126 μm(1.126 mm) at 1269K for 100% hydrogen peroxide. Owing to the exponential nature of the Arrhenius equation, detention like behavior is observed once a critical temperature is reached. Doubling in the Damköhler number correlated to reduction in decomposition length by approximately half, while reducing inlet concentration to 85% increased critical length by about 300 μm and decreased the final temperature to 861K. Variation in the Zeldovich number, corresponding to different catalysts had an effect on critical length that was significant but less so than either of the previous parameters. Overall decomposition lengths were found to be almost ten times longer than in the previous paper. In the last of Zhou's papers on the topic a zig-zag geometry was modeled in 2D[27]. In this paper Region V was modeled in Fluent 6.2 using the previous model for initial conditions resulting in inlet mass fractions of 0.547, 0.24, and 0.213 for H_2O_2, H_2O, and O_2 respectively. The inlet temperature was set at the vaporization temperature of hydrogen peroxide, 423 K. Results from these efforts give an approximate length of 4000μm for complete decomposition in a subregion of the GSFC geometry.

1.4 Current Work

A three section MEMS-based solution has been jointly pursued by NASA Goddard Space Flight Center (GSFC) and the University of Vermont to provide small impulse bit thrust as efficiently as possible. A schematic representation of the effort is shown in Figure 1.9. The first section is an injector that creates "microslugs" of fuel separated

by volumes of inert gas with the goal of reducing the impulse bit as described by McDevitt et al.[17] The second section is the catalytic bed, which will be the main subject covered herein. The last section is a converging diverging nozzle, which has been characterized in depth by Louisos et al.[14] The upstream and downstream conditions of the catalyst bed are determined by the injector and nozzle respectively.

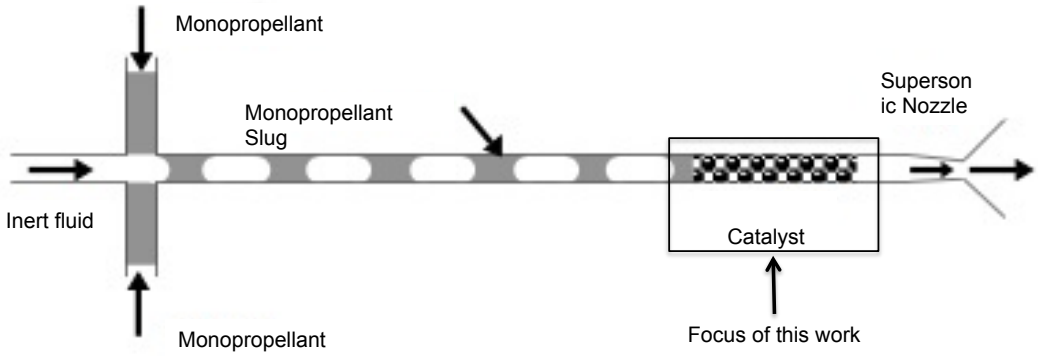

Figure 1.9: Thruster schematic: Depicted above is a schematic representation of the integrated micro thruster that has been proposed. The dark fluid represents H_2O_2 while the white bubbles represent an inert gas. This is done to significantly lower the impulse bit. The slug flow then enters the catalyst bed with exhaust gasses then exits through a supersonic nozzle vented to atmospheric conditions.

This work is part of an ongoing project with the goal of delivering a fully characterized numerical model of a MEMS-based reactor and a corresponding experimental prototype implementing RuO_2 nanorods. This study will explore 0D and 2D computational models of variants of the NASA Goddard configuration in an effort to optimize pillar size and spacing, as well as overall chamber dimensions. Computational models will then be compared with experimental work that has been performed concurrently.

Chapter 2

Computational Methodology

In an effort to optimize the geometry of the catalytic chamber, computational studies were conducted. First, a 0-dimensional model of the chemical kinetics was considered followed by 2- dimensional models of a straight channel and a subsection of the NASA GSFC/ UVM pillar configuration. The straight channel was modeled prior to modeling the pillar configuration in order to ascertain information about critical lengths and modes of head and mass transport on the micro scale. The catalytic decomposition of H_2O_2 is extremely exothermic with the products of the decomposition of 100% being superheated steam and oxygen with an adiabatic flame temperature of approximately 1255 K. Pure HTP is not commercially available; however, 90% is readily available from FMC and other suppliers. The presence of water greatly reduces the flame temperature to 1013 K due to the energy needed to vaporize the water. Peroxide liquid has fairly similar properties to water with a few notable exceptions: the density and viscosity are approximately 1.4 times that of water and its boiling point is 423 K. Once HTP has been vaporized its viscosity very nearly equals that of steam and its density very closely follows the ideal gas law.[16]. During the decomposition of liquid hydrogen peroxide there are three regions. In the first region

both peroxide and water exist in the liquid phase, in the second water is in the vapor phase and peroxide remains liquid, and in the final region both are in the gas phase. For this single phase gas model the initial concentration was determined by the enthalpy needed to heat the peroxide-water mixture from 298 K to $T_{vap}^{H_2O}$, vaporize the water, heat to $T_{cap}^{H_2O_2}$ and vaporize the peroxide. The heat liberated during decomposition is balanced on a molar basis by that needed to vaporize the fluids resulting in a greatly reduced H_2O_2 concentration at the beginning of the gaseous region. Modeling only the gas phase with conditions computed from the vaporization of reactants is not uncommon and has been discussed by Bonifacio and Russo.[4] By calculating the percentage of propellant consumed by heating and vaporization, the model can be simplified from multiphase to single phase. As such the inlet temperature is the vaporization temperature of hydrogen peroxide.

2.1 Inlet Conditions

The resulting initial concentrations were calculated analytically. In an adiabatic system the energy needed to vaporize the system must come from heat released by the decompositions. Assuming 100% wt., the decomposition hydrogen peroxide is defined by:

$$H_2O_2(l) \rightarrow H_2O(g) + .5O_2 + Q \tag{2.1}$$

However for initial concentrations less than 100% equation (2.1) becomes:

$$XH_2O_2(l) + (1 - X)H_2O(l) \rightarrow H_2O(g) + .5XO_2 + Q \tag{2.2}$$

Where X is the mole fraction of hydrogen peroxide. For this application rather than allowing the reaction to go to completion, the equation can be written in terms of

moles of peroxide remaining, n:

$$XH_2O_2(l) + (1-X)H_2O(l) \rightarrow nH_2O_2(g) + (1-n)H_2O(g) + .5(X-n)O_2 + Q \tag{2.3}$$

Heat release calculated on a molar basis equates to a change in enthalpy and can be defined as the difference in the heat of formation of the reactants and the products plus the change in enthalpy of the products from the initial temperature to the final temperature. Note that $H_f^{O_2} = 0$.

$$Q = \Delta_f H^{reactants} - (\Delta_f H^{products} + \Delta H_{T_{F-I}}) \tag{2.4}$$

$$Q = \left[X\Delta_f H_{liq}^{H_2O_2} + (1-X)\Delta_f H_{liq}^{H_2O}\right] -$$
$$\left[n(\Delta_f H_{gas}^{H_2O_2} + \Delta H^{H_2O_2}) + (1-n)(\Delta_f H_{gas}^{H_2O} + \Delta H^{H_2O}) + .5(X-n)(\Delta_f H_{gas}^{O_2} + \Delta H^{O_2})\right] \tag{2.5}$$

Setting heat released to zero (Q=0) determines the exact point where the energy released equals the energy needed to vaporize the solution in terms of moles of H_2O_2 remaining.

$$n = \frac{\left[X\Delta_f H_{liq}^{H_2O_2} + (1-X)\Delta_f H_{liq}^{H_2O}\right] - \left[\Delta_f H_{gas}^{H_2O} + \Delta H^{H_2O} + .5X\Delta H^{O_2}\right]}{(\Delta_f H_{gas}^{H_2O_2} + \Delta H^{H_2O_2}) - (\Delta_f H_{gas}^{H_2O} + \Delta H^{H_2O}) - .5\Delta H^{O_2}} \tag{2.6}$$

For 90% hydrogen peroxide X=.8266. Using known values for the heat of formation of liquid and gaseous peroxide and water, as well as, the change in enthalpy from $T_i = 298\ K$ to $T_f = T_{cap}^{H_2O_{@}} = 423\ K$ n is determined ($n = .2836$) resulting in 0.2836, 0.7164, and .2715 moles of H_2O_2, H_2O, and O_2 respectively. These values have been divided by the volume occupied by 1 mole of gas at the reservoir condition (P= 1 atm, T= 298 K) to convert from mole fraction to molarity.

The velocity inlet is a design parameter determined by target thrust. To facilitate modeling of subregions of the domain in 2 dimensions, velocity is chosen rather than mass flow rate with the relationship $\dot{m} = \rho v A$ where the density ρ is estimated to

be $1000kg/m^3$ and cross sectional area A is determined by the overall geometry. Maximum thrust can be determined from the specific impulse and mass flow rate of the fuel.

$$F = I_{sp}\dot{m}g_0 \tag{2.7}$$

Theoretical specific impulse can be determined from inlet conditions and the stagnation temperature T_0 with the relationship:

$$I_{sp} = \sqrt{\frac{2\gamma RT_0}{g_0^2(\gamma - 1)}} \tag{2.8}$$

For the target thrust range from 1-500 μN based on the GSFC prototype the channel width is fixed at 1103 μm; however the etch depth can be varied. Therefore for a fixed specific impulse ($I_{sp} = 185s$)[11] and channel width, thrust can be varied by either changing velocity or etch depth. For a fixed etch depth of 100 μm thrust varies from 20 μN to 500 μN for velocity of 0.1 $\frac{m}{s}$ to 2.5 $\frac{m}{s}$, respectively. Conversely, if velocity is held constant at 1 $\frac{m}{s}$, thrust ranges from 20 μN to 1000 μN for depths of 10 μm to 500 μm. Owing to the two-dimensional nature of this study Figure 2.1 shows thrust per unit depth. The default case for this study will target 10 $\mu N/\mu m$, with an inlet velocity of 0.5 m/s. For parametric studies, inlet velocity will be varied from 0.1 to 2.5 m/s.

2.2 Governing Equations

The chemical kinetics and reaction rate have been calculated using the Arrhenius equation (2.10). Activation energy (E_a) is the energy needed for the reaction to move forward. The introduction of a catalyst drastically reduces this value from $200\frac{kJ}{mol}$[10] to $50.2\frac{kJ}{mol}$[27]. The pre-exponential factor (A) is a scaling with units of s^{-1} and

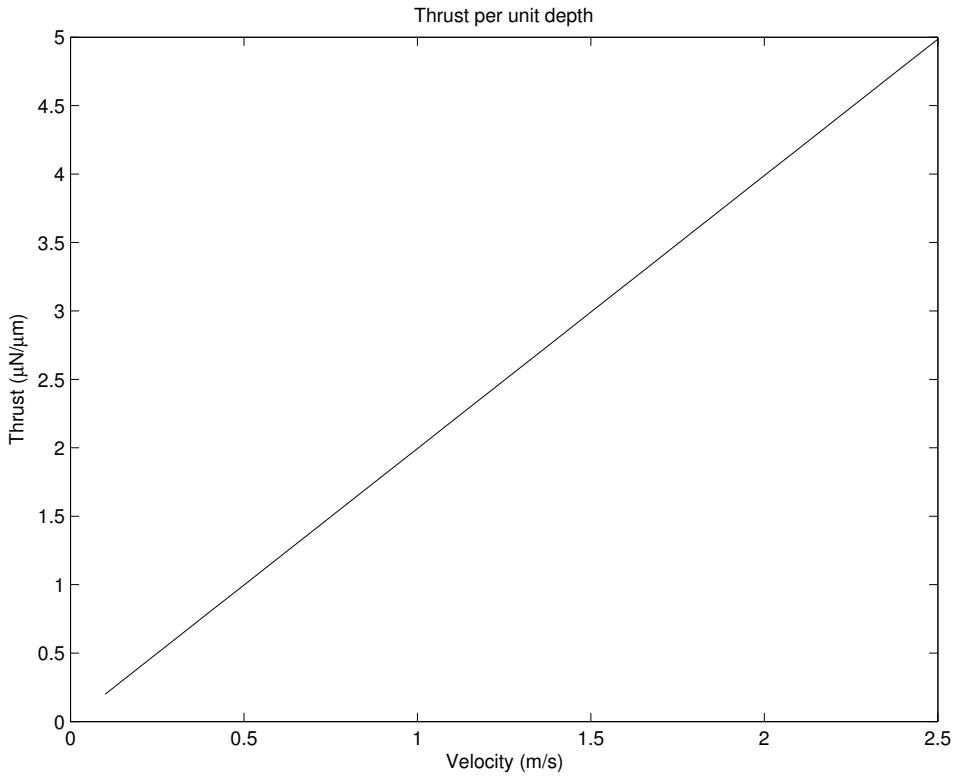

Figure 2.1: Thrust is determined by cross sectional area and mass flow rate. When velocity varies from 0.1 to 2.5 m/s for a fixed cross sectional area, thrust varies linearly. A linear variation is also observed when holding flow rate constant and changing the etch depth. In a 2D model non- dimensional depth removes consideration of the third dimension and can be a better metric. The dependent variable is now measured in μN per unit depth.

varies as a function of surface area to volume ratio. For the given configuration Zhou estimated $A = 10^9 s^{-1}$. These values are inline with what is expected according to collision theory.[3]

$$H_2O_2 \rightarrow H_2O + \frac{1}{2}O_2 + Q \tag{2.9}$$

$$k = A \exp\left(\frac{-E_a}{RT}\right) \tag{2.10}$$

$$r = kC_{HTP} \tag{2.11}$$

Comsol Multiphysics 4.2a uses finite element analysis to solve the compressible, unsteady Navier-Stokes equations (2.12 & 2.13) coupled with mass balance equation (2.14), the heat equation (2.15) and the Arrhenius equation(2.10).

$$\rho\frac{\partial \mathbf{u}}{\partial t} + \rho(\mathbf{u}\cdot\nabla)\mathbf{u} = \nabla\cdot[-\rho\mathbf{I} + \mu(\nabla\mathbf{u} + (\nabla\mathbf{u})^T) - \frac{2}{3}\mu(\nabla\cdot\mathbf{u})\mathbf{I} + \mathbf{F} \tag{2.12}$$

$$\frac{\partial \rho}{\partial t} + \nabla\cdot(\rho\mathbf{u}) = 0 \tag{2.13}$$

$$\frac{\partial c_i}{\partial t} + \mathbf{u}\cdot\nabla c = \nabla\cdot(D_i\nabla c_i) + R_i \tag{2.14}$$

$$\rho C_p\frac{\partial T}{\partial t} + \rho C_P\mathbf{u}\cdot\nabla T = \nabla\cdot(k\nabla T) + Q \tag{2.15}$$

$$\rho_i = \frac{P}{R_s T} \tag{2.16}$$

$$R_s = R_{const}/\frac{M_{H_2O_2}C_{H_2O_2} + M_{H_2O}C_{H_2} + M_{O_2}C_{O_2}}{C_{H_2O_2} + C_{H_2O} + C_{O_2}} \tag{2.17}$$

Initially material properties are determined from the bulk concentration on a molar average. The effects of variations in properties across the flow are studied to determine the necessity of mass averaged settings. Density is calculated using the ideal gas law(2.16) with a mean molar mass determined from the local concentration. The nanorod geometry is ignored and modeled as a surface coating. They can be accounted for at a later time by adjusting the pre-exponential factor to match experimental results.

2.3 0D Model and Preliminary Simulations

Comsol Multiphysics and the Chemkin input package were used to develop a non-dimensional model of the reaction taking place on the surface of the model. This model assume a stationary flow with diffusion and determines temperature and local concentration of species at a point on the surface as a function of time, representing the residence time needed for decomposition. This was done to validate the input parameters of the Arrhenius equation and to determine their effects. Parametric studies are conducted to determine its impact of activation energy and the pre-exponential factor on residence time for complete decomposition.

2.4 2D Model of a Catalytic Wall

A slender straight channel ($10\mu m \times 5mm$) was modeled to apply the reaction kinetics to a fluid flow in order to determine decomposition lengths rather than residence times. The flow is assumed to be unidirectional and the geometry lacks all complexities of the actual catalyst bed geometry. The inlet is a laminar inflow condition and has been set to a prescribed temperature of 423 K. Species inflow is as stated previously. The top of the channel has been set as a symmetry boundary condition. The first $25\mu m$ of the bottom is set as an insulated wall and the remainder is the catalytic surface. This has been done to prevent heat from being conducted upstream through the boundary. The outlet is a pressure outlet (1 atm). This is the only mode for heat to exit the system. This study was conducted to analyze the effects of material properties without the effects of geometry. Here viscosity, mass diffusion and thermal conductivity are studied. Inlet velocity is also varied to determine its effect on decomposition length. A grid convergence study of this domain shows that the domain

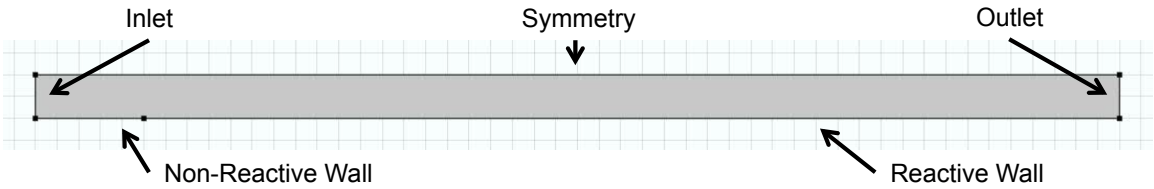

Figure 2.2: Shown is a representation of the numerical domain. The top wall is a symmetry condition and the bottom is a no-slip wall condition. The first 25 μm of the bottom wall is non-reactive to prevent a discontinuity at the inlet. The inlet is a laminar inflow condition with an average velocity of 1.0 m/s at a prescribed boundary temperature of 423 K for the standard case. A pressure outlet at atmospheric conditions is used.

is not grid sensitive. A point monitor of pressure in the domain located at (5, 3750) shows a difference of 0.0317% from the least refined to the most refined mesh. Table 2.1 shows the effect of grid refinement on the model.

Table 2.1: Grid refinement study based on maximum element size with most refined on the left and least refined to the right.

Maximum Element Size [μm]	Degrees of Freedom	Elements
2.5	226,059	8,000
2.25	362,760	13,350
2.0	466,265	15,006
1.75	710,679	17,160
1.5	852,111	32,000
1.25	1,315,137	50,000

2.5 2D Model of Catalytic Pillar Geometry

Preliminary results from the simplified 2D model were used to model a sub-region of the NASA GSFC/ UVM pillar geometry. The standard case consists of a half row of pillars. Each pillar has a square cross section with 40 μm sides that are spaced 20 μm apart. This represents 1/26 of the full domain. For a parametric study of pillar

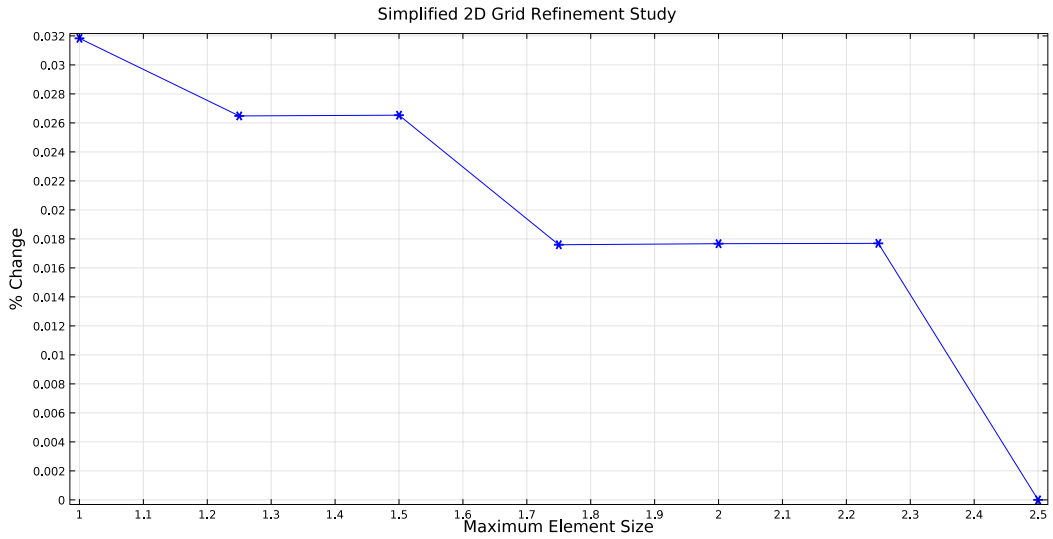

Figure 2.3: Plotted is a point monitor of pressure located at (5,3750). Percent change is calculated as $(p - p_0)/p * 100$ where p_0 is the pressure of the least refined grid considered. The plot should be considered as the most refined mesh on the left to the least refined mesh to the right. A maximum difference of approximately 0.032% is seen from these extremes. For the remainder of the study a maximum element size of $2.0\mu m$ is chosen resulting in 15,006 elements.

size the overall channel width is held constant at 42.24 μm or 1/26 of the original channel width, 1103 μm. All horizontal faces are modeled as a symmetry condition. The sides of each pillar are defined as reactive walls. The inlet is a laminar inflow with an average velocity of 1.0 m/s for the standard case. The outlet is a pressure condition at 1 atm. Figure 2.4 shows a reduced domain to identify key dimensions and areas.

The domain has been broken down into rectangular regions to enable the use of a mapped meshing scheme. A triangular region at the inlet and the outlet is necessary and is mapped using free triangles. Figure 2.5 shows how this was accomplished. Subfigure (b) shows the inlet, (c) the outlet, and (d) an interior region.

A grid convergence study was conducted for the standard geometry of 40 μm sided pillars. The element size was then held constant for all other geometric permutations.

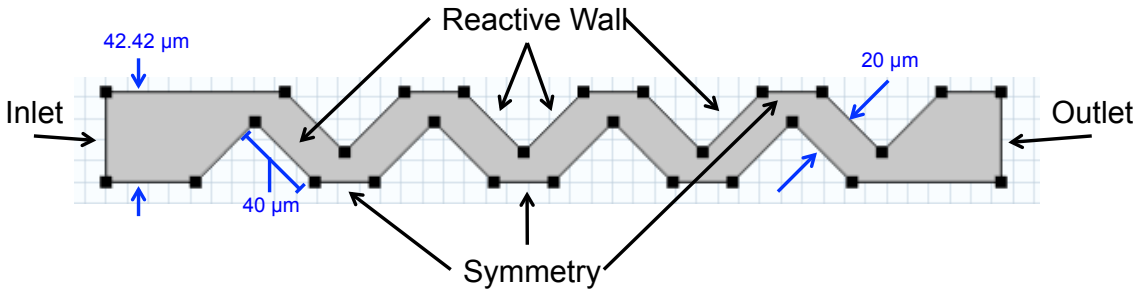

Figure 2.4: A reduced domain is shown for clarity. The diagonal walls are the pillar sides and are defined as reactive walls. All horizontal walls are set as symmetric as this is intended to be an interior region of a larger array. The inlet condition is laminar inflow with an average velocity of 1.0 m/s for the standard case. The inlet is set to a prescribed temperature of 423 K as previously justified. The outlet is a pressure condition at 1 atm.

The grid convergence study showed that the model was grid insensitive for a maximum element size under 2 μm and this was accepted as the metric for resolution needed.

Table 2.2: Grid refinement study based on maximum element size for pillar configuration

Maximum Element Size [μm]	Degrees of Freedom	Elements
2.25	371,657	14,867
2.0	486,089	19,532
1.75	623,383	25,187
1.5	825,886	30,492

Several parameters were studied to determine their effects on critical length, exit velocity, and exit temperature. While thermal conductivity is a material property that cannot be changed, studying its effect by comparing non-conductive flows with more realistic flows can provide insight into the role conduction plays in the flow. Activation energy is another intrinsic property of the system. This value, however, is not explicitly determined for this system and values vary widely in the literature. A reasonable value of 52.4 kJ/mol is chosen as the standard case. The effect of activation energy will be studied parametrically to show how fine-tuning this value can be used

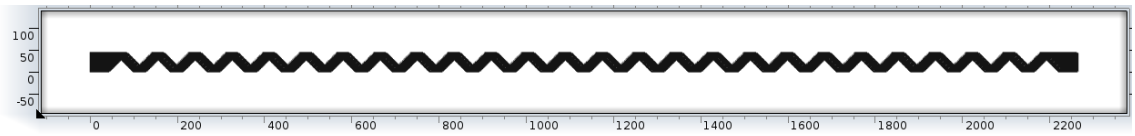

(a)

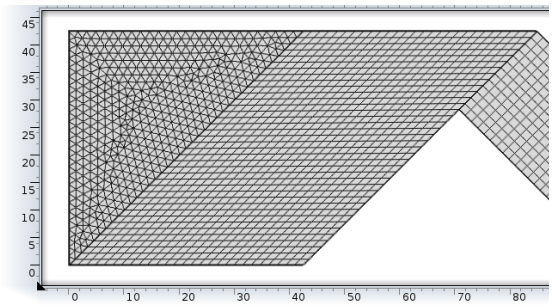

(b)

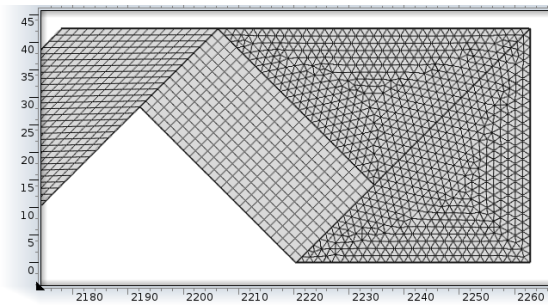

(c)

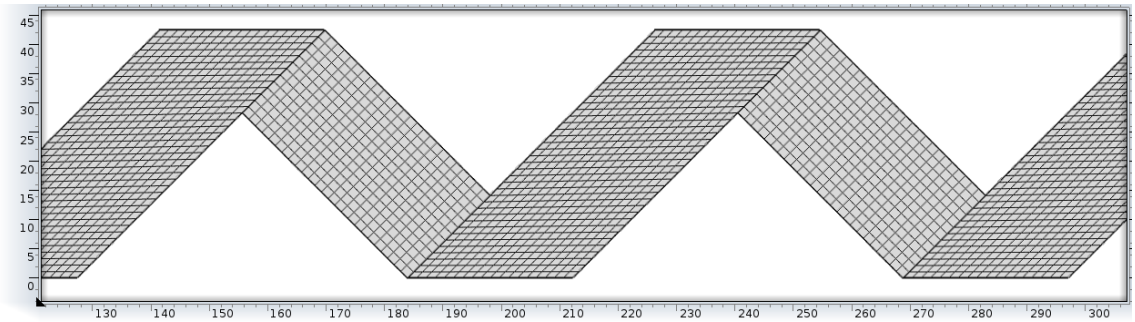

(d)

Figure 2.5: (a) An illustration of the overall domain that has been meshed. Here it can be seen that the domain is approximately 50 μm wide by 2200 μm long. Figures (b)&(c) show the areas that have been meshed with free triangles to complete the domain at the inlet and outlet of the domain respectively. (d) The interior of the domain has been broken into subregions to allow for a mapped grid.

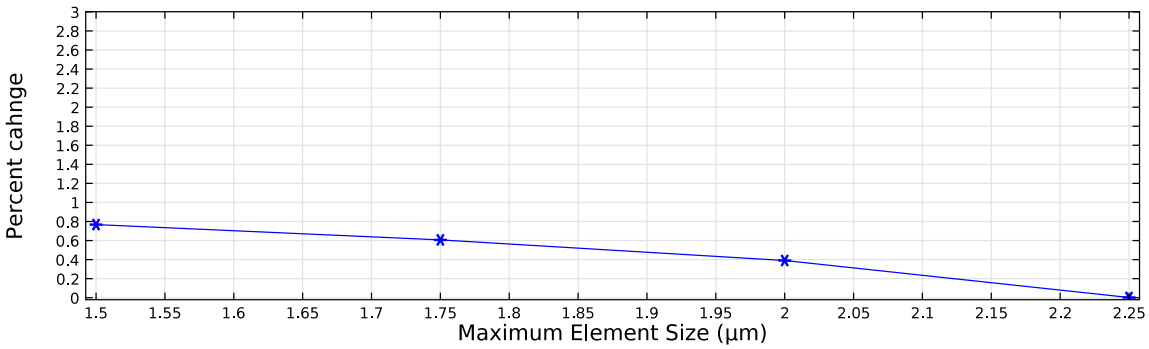

Figure 2.6: Mole fraction was averaged over the exit plan for the highest inlet velocity case, 2.5 m/s. The average value is plotted verse maximum element size. When normalized by the value for the coarsest grid a variation of less than 1% is observed. A modest maximum element size of 2 μm will be used for studies.

to better correlate computation models with experimental data. If a model can be well correlated with a matching experiment, the model becomes much more useful for predicting optimal dimensions. Lastly inlet velocity is varied based on target thrust levels as discussed previously. This will help to predict the critical length required for different applications and to allow for an application specific reactor to be designed.

Chapter 3

Experimental Methodology

Meso-catalyst beds using ruthenium oxide powder and micro catalyst beds with RuO_2 nanorods were fabricated and tested to show the effectivity of RuO_2 as a catalyst and the robustness of nanorods against temperature and pressure. There is the possibility of RuO_2 being further oxidized to RuO_4 with prolonged use; this will be characterized experimentally. Decomposition and vaporization occur much too rapidly to capture via standard video frame rates. The use of high-speed photography provides valuable insight into the reaction mechanism. The Phantom© v310 camera developed by Vision Research Inc. was used to visualize the fluid flow. The camera has a maximum resolution of 1280 by 800 pixels. It is capable of frame rates up to 500,000 frames per second at reduced resolutions. Micro Epsilon Compact Thermal Imager™ was utilized to provide temperature data during each run. The camera has a maximum resolution of 160 by 180 pixels. Labview was used to operate the pump while recording dispensed volume and temperature measured by the thermocouple.

3.1 Meso-Scale Reactor

The preliminary goal is to design a low cost meso-scale hydrogen peroxide thruster for the Ruthenium Oxide catalyst to provide a proof of concept for ongoing research toward an integrated micro propulsion system. Using off-the-shelf components a pump fed thruster was assembled consisting of assorted fittings and tubing. In the preliminary stages $\frac{1}{16}$ inch od. capillary tubes were used for the catalyst section to allow for observation. The glass tubes required the use of plastic fittings. The capillary tubes were later replaced by stainless steel tubing to accommodate the high temperatures as well as metal fittings. Powdered RuO_2 was held in place by a $0.5\mu m$ porosity filter. Some tests were performed with a rapid prototyped conical nozzle with a 1 mm throat fitted to the end of the catalytic chamber. High-speed imagining was used to obtain visual data from each run at 60 fps and full resolution.. The high speed camera was positioned horizontally looking at the side of the thruster and the thermal imager was oriented vertically viewing the top. This was done to remove any loss of prospective associated with angular distortion. The glass and stainless steal thrusters can be seen in Figure 3.1(a) and 3.1(b) respectively.

3.2 MEMS-Based Reactor

A microreactor was studied with the ultimate goal of delivering a MEMS RuO_2 based catalytic reactor. First, configurations to replicate subsections of the NASA Goddard design were made. Several configurations were considered, the approximate dimensions of which are given in table 3.1. Channel (a) and (c) are slender channels with an overall width of approximately 100 μm while (b) and (d) are significantly wider at approximately 500 μm. From these designs, lithographic photomasks were made and

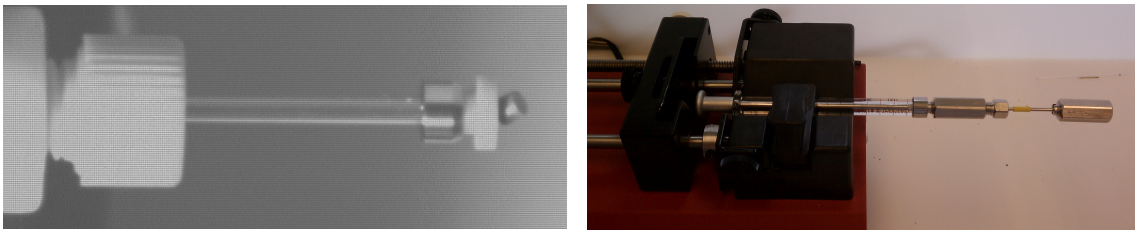

(a) (b)

Figure 3.1: (a)An example of the mini thruster constructed with off-the-shelf parts. Here the catalytic chamber is a glass capillary tube. Notice at the far right of the thruster, the filter used to prevent RuO_2 powder from being carried out by the exhaust gases has been pushed out of place. (b) This prototype was constructed out of stainless steel(except the glass syringe) to overcome temperature and pressure failures that occurred with previous models. The drawback of using metal tubing is the loss of visual access to the chamber.

used to etch the channels using deep reactive ion etching (DRIE) methods. Figure 3.2 is a flowchart representation of photolithography. The silicon wafter comes from the manufacturer with a thin silicon oxide layer. During DRIE the silicon substrate etches 100 times faster than the oxide layer allowing for the areas with the thin film to remain unaffected by the etch. DRIE works by using photolithography to remove portions of this layer. To do so the substrate is first coated in positive photoresist by a spin coating technique. After the wafers are coated with resist, they are subjected to a soft bake (85°C) for 15 minutes, and subsequently exposed to UV radiation through a mask for 20 seconds. Following exposure, the resist film undergoes development using the RR6 developer in order to leave behind an image which will serve as a mask for etching, this is followed by a deionized water rinse. The wafers are baked to a temperature of 120°C for 30 minutes leaving the prescribed pattern. For dry etching, Deep Reactive Ion Etching (DRIE) was used. It has the capability of achieving a aspect ratio of 30:1 and silicon etch rates as high as $2\mu m/min$.[1]. SEM images of the Pillars (Figure 3.5(a)) show the precision to which these geometries can be produced.

Next RuO_2 nanorods were grown on the pillars, see Figure 3.5(b). Nanorods seemed to prefer the pillar sidewalls rather than the bottom surface of the substrate as can be seen in Figure 3.6(a). While this is not ideal because it means essentially wasting valuable surface area, it is likely to correlate better with the numerical model which ignores the lower surface. Figure 3.6(b) shows the high density of nanorods grown on the pillar walls.

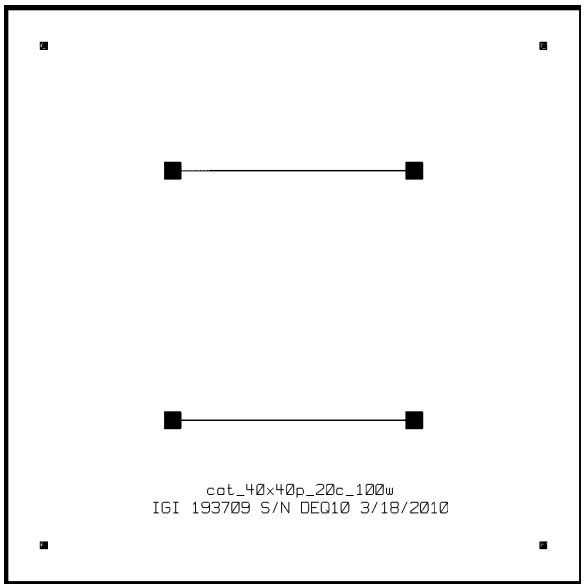

Figure 3.2: This is one of the 4 different soda lime photomasks generated. The area to be masked is coated in chrome. Each mask is square with 4 inches per side and is 0.06 inches thick. The usable area is limited to a 3 inch diameter circle by the silicon wafer. Tolerances of +/- 0.05 μm are guaranteed by the manufacturer.The large squares on either end of each channel are reservoirs where ports will be attached.

Finally, the silicon substrate was fixed to a glass coversheet with pre-drilled holes by anodic bonding. Anodic bonding is a process of permanently affixing glass to silicon by heating and subsequently passing current through the materials. Figure 3.7 shows how the procedure is done.

For this experiment, liquid H_2O_2 was fed in much the same way as the mesoscale experiment. Again high-speed video with microscopic lenses was used to observe the

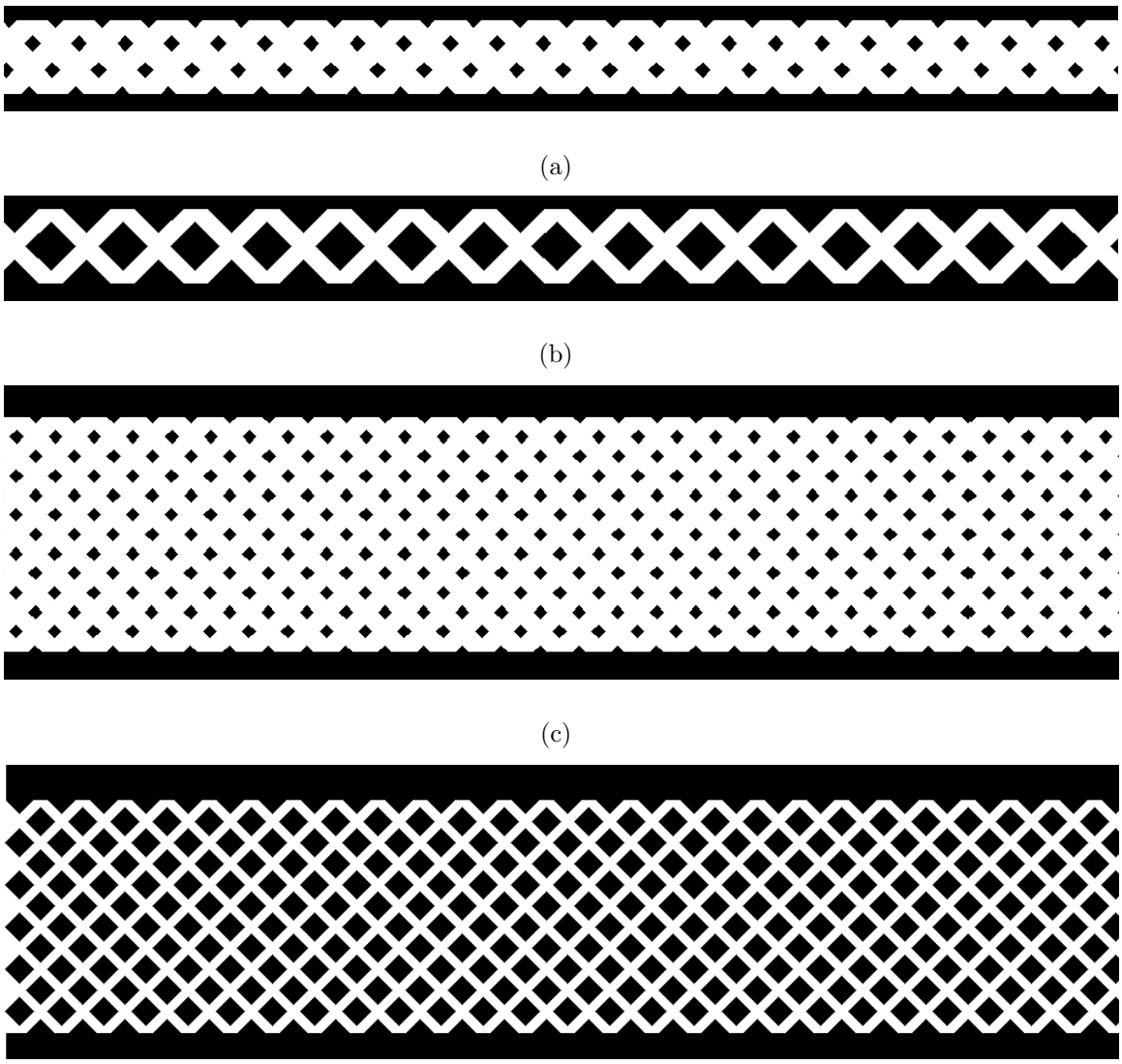

(a)

(b)

(c)

(d)

Figure 3.3: Proofs of the design were provided and are shown here. In all, masks for 4 different geometries were made. See 3.1 for specific dimensions. Different designs were considered to help determine which most efficiently decomposes the fuel. Narrow channels aimed at determining effects of surface tension while the wider channels targeted the more accurately recreated test by NASA Goddard.

Table 3.1: Mask geometries corresponding to Figure 3.3

	Pillar side length	pillar spacing	# rows
(a)	20 μm	40 μm	2
(b)	40 μm	20 μm	1
(c)	20 μm	40 μm	11
(d)	40 μm	20 μm	10

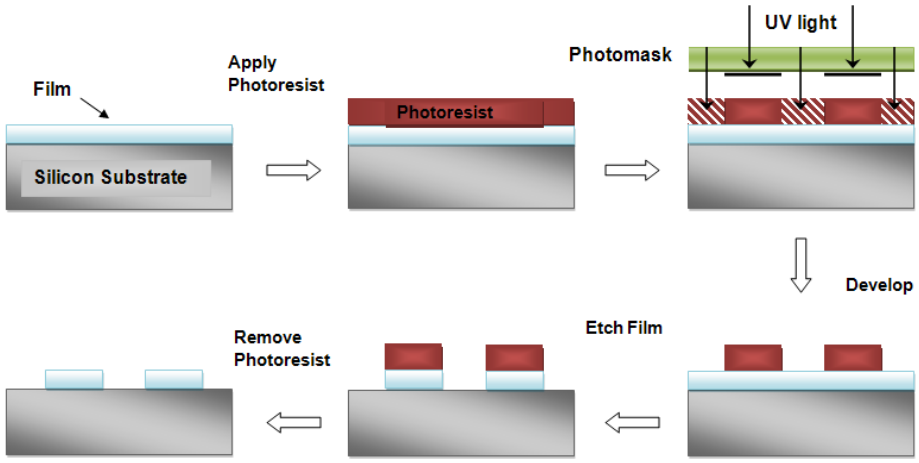

Figure 3.4: This flowchart represents the processes involved in photolithography. The silicon wafter comes with a thin oxide film which is etched 100 times more slowly than silicon. First layer of photo resister is added. The photomask is then put in place over the photoresist. Ultraviolet light is then applied which removes the photoresist not protected by the mask. The pattern is then developed using standard photographic developing procedures. This allows for inspection of the patterning. A wet etch is then performed to remove the thin oxide layer not covered with photoresist. After the photoresist is removed only the pattern from the photomask is left in the thin oxide layer. The substrate is then ready for DRIE to be performed.

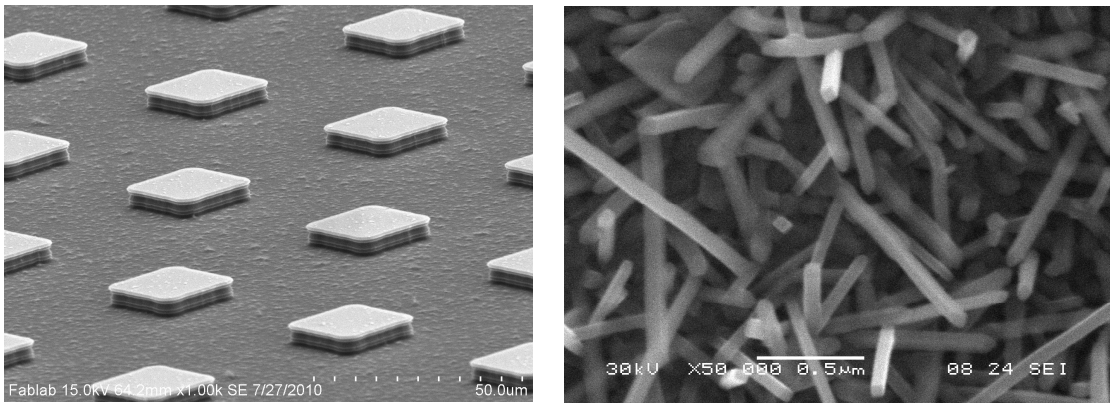

(a) (b)

Figure 3.5: (a) This SEM photograph highlights the precision fabrication that is possible. The pillars are 20 μm on a side with 40 μm spacing. (b) Here is an image of densely packed nanorods. The scale bar in the center of the photo is 0.5 $\mu mlong$. Nanorods will greatly increase the surface area available for surface reactions by extending away from the wall into the flow. The pillars will then act as a scaffolding for the nanorods.

flow. Thermal imaging and thermocouples were used to monitor temperature in the channel. Images presented in this study were captured at 33,000 fps with a resolution of 1024 by 960 pixels. Here reducing resolution allowed for decreased exposure time and therefore higher frame rate. The narrowness of the channel allowed the reduced vertical field of view without the loss of quality. The camera was positioned above the channel looking down. The channel was affixed to a 3-axis stage allowing for precision placement and focusing. After configuring the capture settings, the camera was triggered to begin recording. The resulting high-speed video captured the fluid flow and reaction mechanics. Figure 3.8(a) demonstrates a typical experimental setup for high-speed photography. In the center of the photo the placement of the channel is noted. See figure 3.8(b) for an enlarged view of the test section. The experimental arrangement shown in the figure also utilizes the Micro Epsilon Compact Thermal Imager. The camera has a maximum resolution of 160 by 180 pixels. The goal of

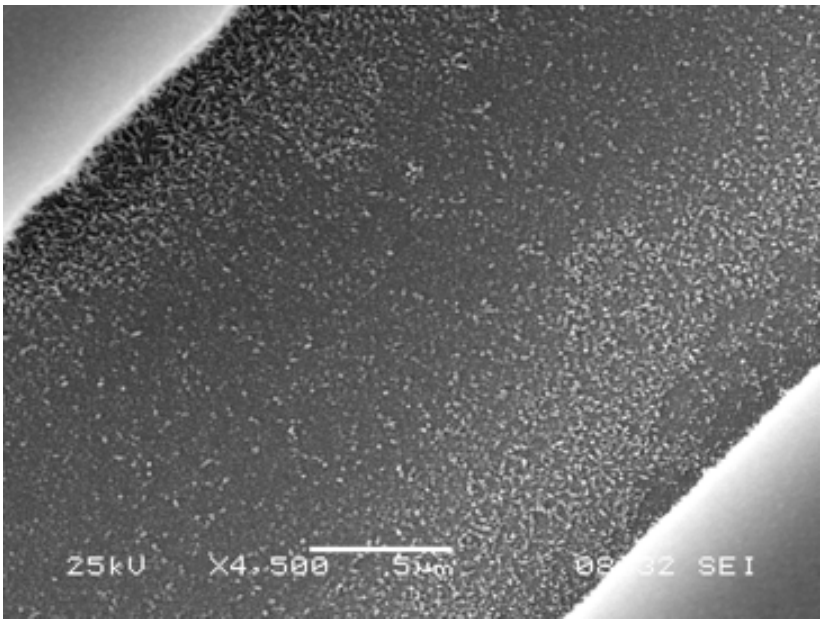

(a)

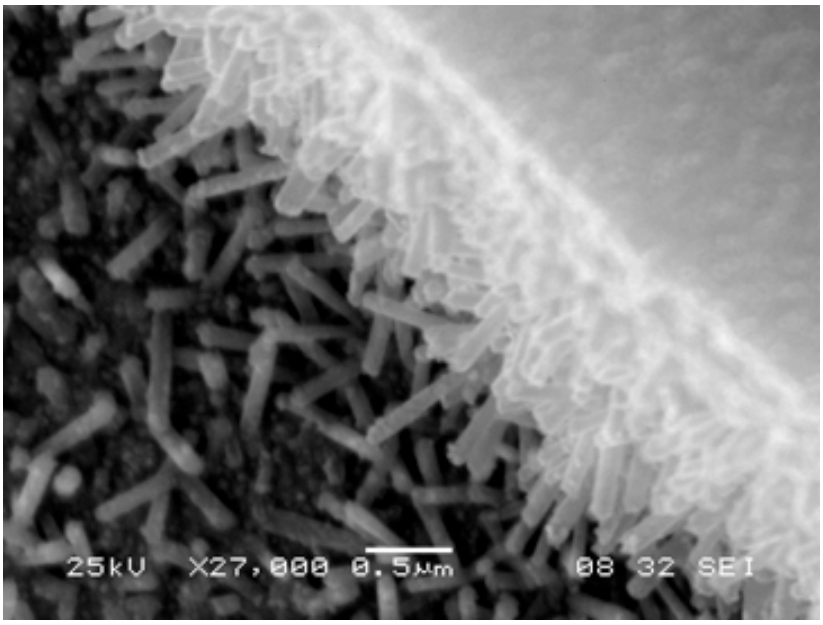

(b)

Figure 3.6: (a) This image shows that nanorods were grown in much higher density close to the channel walls and on the walls than in the center of the figure. Nanorods are the white specks in the image. The darker region near the wall is the result of a shadow. (b) A close-up of the pillar highlights the high growth density in this region. The dark surface is the channel bottom and the lighter surface is the pillar wall and top surface of the pillar.

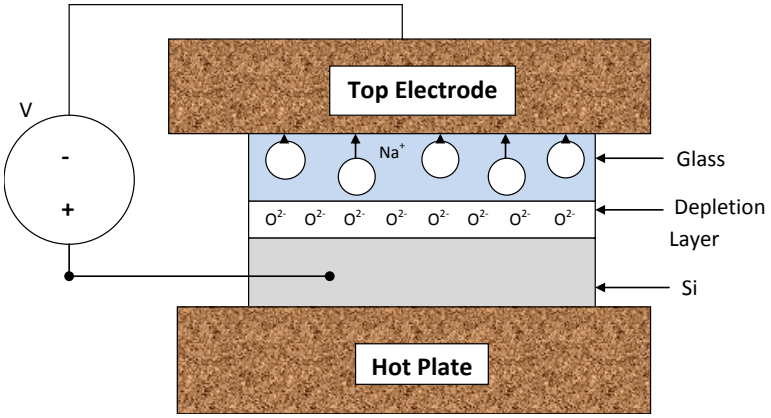

Figure 3.7: Anodic bonding is the process by which glass is bonded to silicon by heating and passing current thorough the materials. When the voltage is applied sodium ions in the glass are pulled toward the cathode leaving negatively charged oxygen ions to bond with the silicon wafer. Image provided by Asante[1]

thermal imaging is to determine if isolated heating occurs at the surface creating non-uniform temperature distributions along the flow. Also a maximum temperature observed in the flow would signify the completion of decomposition.

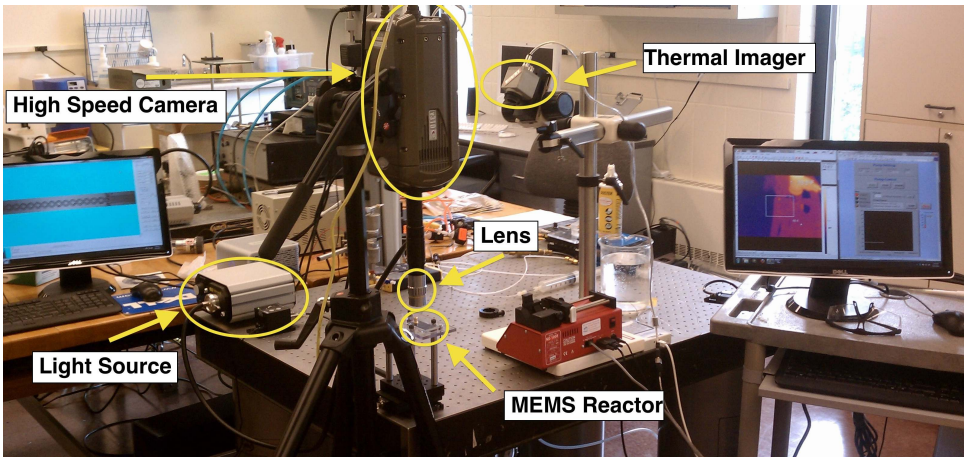

(a)

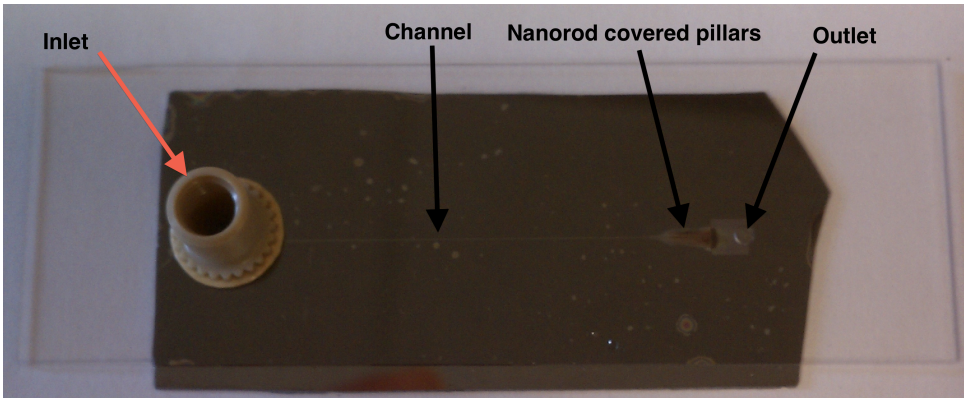

(b)

Figure 3.8: (a)The experimental setup utilizes high speed photography (center) looking down on the stage. In the monitor on the left hand side of the image the channel can be seen. The high sped camera is equipped with an infinity tube and light source to ensure full exposure on a very short time scale. Magnification can be varied from 5x to 100x based on the investigation being performed. The monitor to the right shows output from the thermal imager and the Labview GUI used to operate the syringe pump. (b) This is an example of an anodically bonded channel with nano rod covered pillars.

Chapter 4

Computational Results

Computational models provided insight into the complexities of catalysis that were not evident at the onset of the project. These include axial conduction of heat in the fluid, as well as, the effects of ternary mass diffusion to changes in density related to temperature and concentration. These considerations combined with kinetic parameters lend themselves to parametric modeling. For this engineering design project exact values for different properties and parameters are unknown and often unattainable. Rather than perform complex experiments beyond the expertise and resources available, a "bracketing" approach was taken. Reasonable upper and lower bounds were determined for several key properties. These bounds were then modeled to determine the magnitude of their effect on critical length and temperature.

4.1 0D Model

Using the reference set of parameters an adiabatic flame temperature of 1005.5 K is reached; which is very close to the published value of 1013 K [16]. A detonation type behavior is observed when a critical temperature is reached, as would be expected

due to the exponential nature of the Arrhenius equation (2.10). This temperature is approximately 550 K for the parameters used, which is reached in 10^{-3} seconds due to the elevated initial temperature associated with the preheated inlet condition in our studies. The Activation energy was varied to determine the effect of the chosen catalyst on the required residence time. Figure 4.1(a) shows this relationship. Activation energy is not affected by geometry or operating conditions and therefore will be held constant for the remainder of the study. A parametric study of the pre-exponential factor shows that while this value has a significant effect on the kinetics of the reaction, values above 10^7 only affect residence times on the order of milli seconds, Figure 4.2(a).

4.2 2D Model of a Catalytic Wall

At low flow rates ($\approx 0.1\ \frac{m}{s}$) conduction dominates heat transfer and heat can be conducted upstream. With average conductivity heat is conducted upstream of the beginning of the catalytic region resulting in a preheating of the flow. This also results in a slightly reduced exit temperature when compared to the 0D model. For an essential non-conductive flow there is a drastic temperature increase at the leading edge of the catalytic region resulting in rapid decomposition; however, heat is not able to travel from the surface resulting in a lengthened decomposition length. From $k = 1.0 \times 10^{-4}$ to $k = 3.8 \times 10^{-3}$ the mode of heat transfer transitions from convection to conduction which drastically changes the flow (Figure 4.3(a)). Once conduction dominates, increasing conductivity decreases decomposition length by preheating inlet gas before it reaches the catalytic bed, but decreases exit temperature. Comparing contours of mole fraction for non-conductive (Figure4.3(b)) and conductive (Figure 4.3(c)) flow shows how the change in heat transfer effects the reaction rate. Viscosity

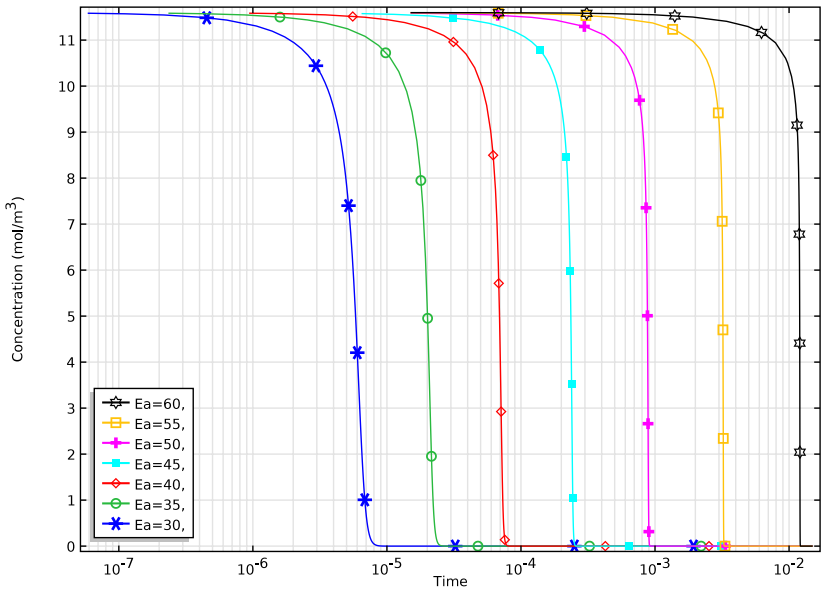

(a)

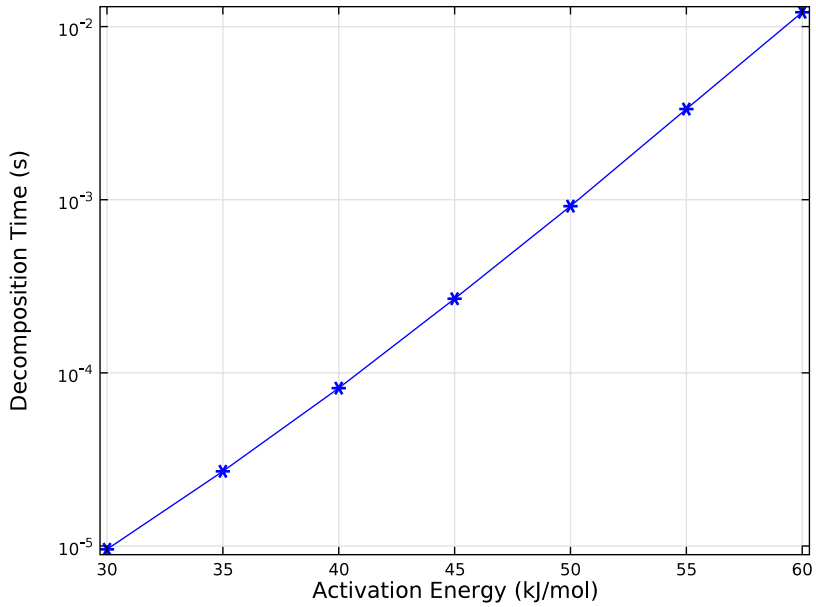

(b)

Figure 4.1: (a) This plot depicts the detonation type behavior arising from the exponential nature of the Arrhenius equation. With the initial temperature of 423 K there is sufficient energy for the reaction on the necessary time scale as the E_a is below 50 kJ/mol. Here it can be seen that even a reduction in activation energy of 10% can reduce the residence time by half. (b) Plotting the the zero value for each activation energy verse time on a semi log axis shows the exponential behavior of the Arrhenius equation.

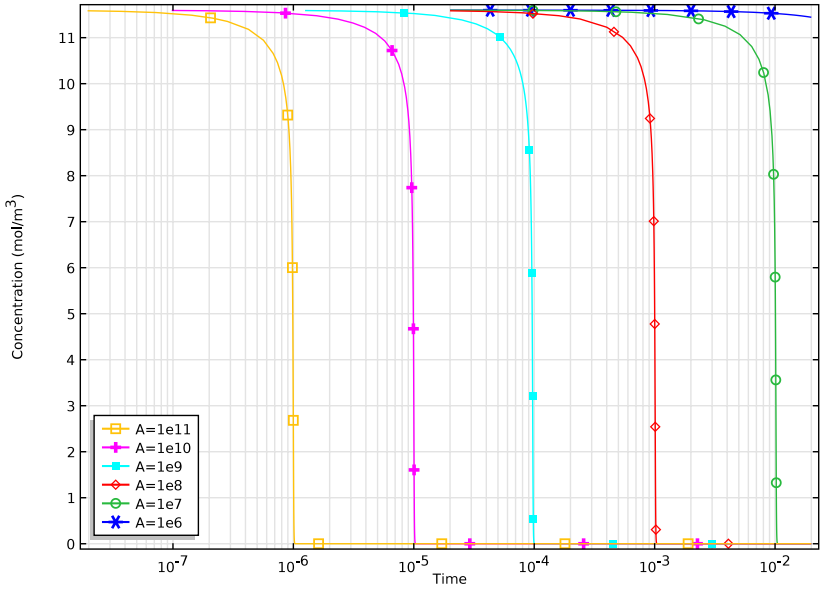

(a)

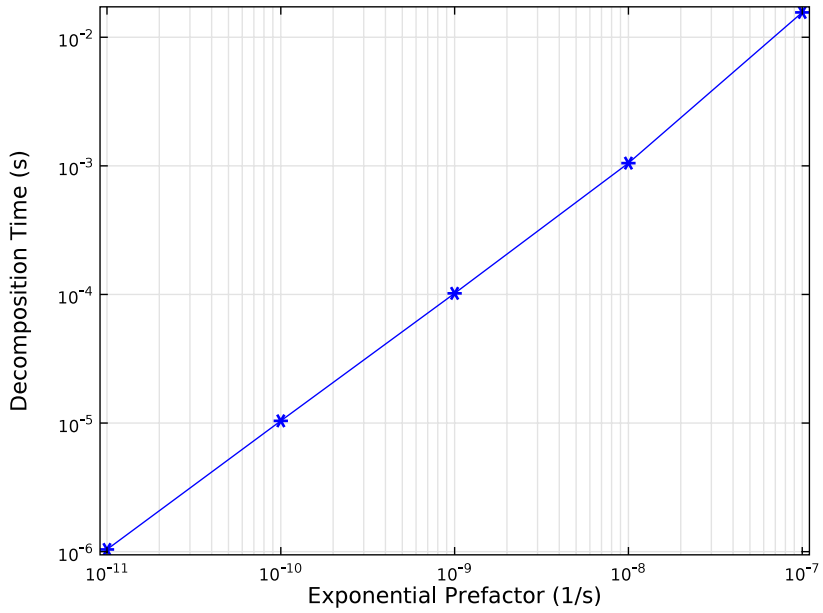

(b)

Figure 4.2: (a) Values for the exponential prefactor vary widely in the literature due to the dependance on geometry. This value will require experimental input as it significantly affects the time scale. (b) Plotting the critical time over the range of values on a log-log axis shows the linear relationship between the exponential prefactor and critical time. $A = 10^{-8}$ will serve as the standard case.

was varied from inviscid to artificially high viscosity. This resulted in effectively no change in decomposition length, see Figure 4.4. This demonstrates that viscous diffusion does not play a significant role species transport which is dominated by mass diffusion.

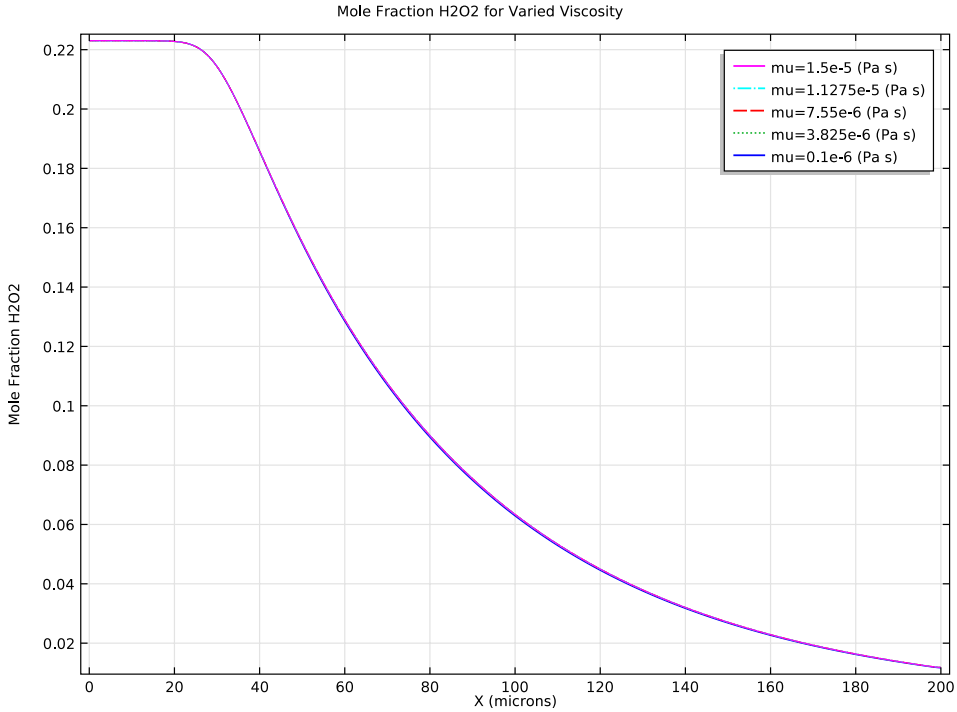

Figure 4.3: The effect of viscous diffusion is negligible. As viscosity varies from nearly inviscid ($\mu = 1.0\times10^{-6}$) to typical values for hydrogen peroxide ($\mu = 1.5\times10^{-5}$) no changes in species transfer can be seen. This signals that viscous diffusion does not play a significant role in species transport, which is dominated by mass diffusion.

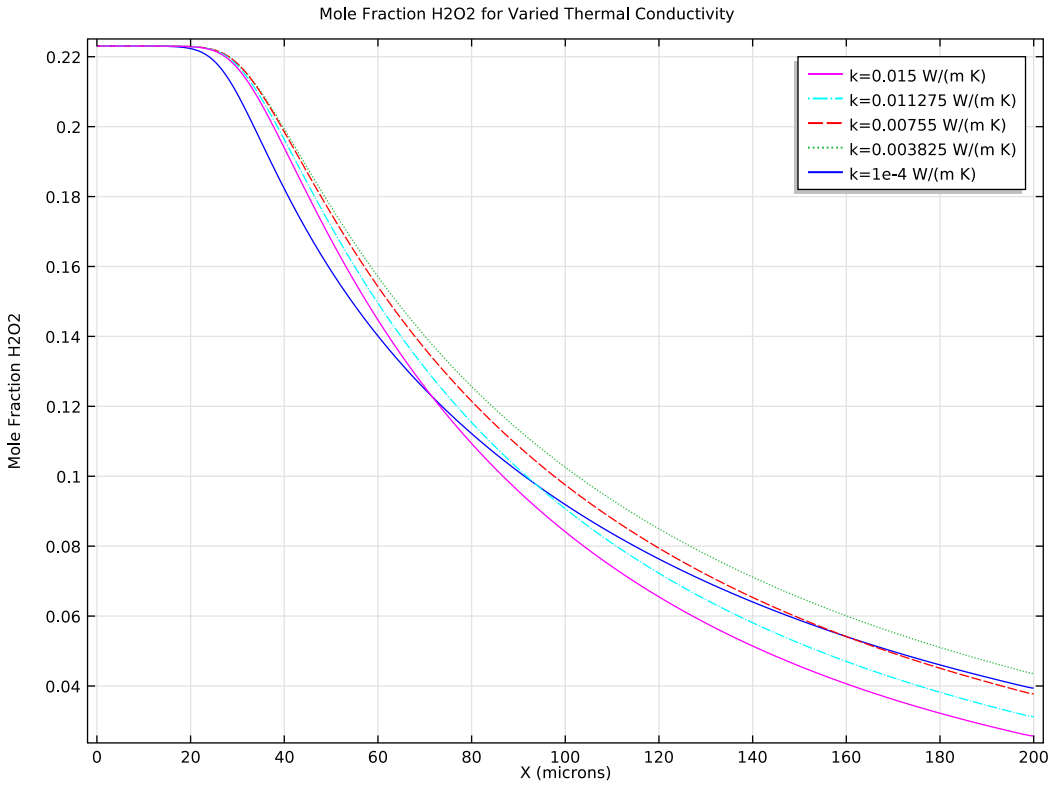

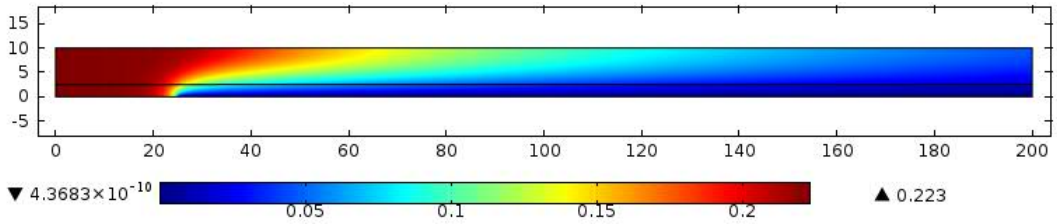

(b) $k = 1 \times 10^{-4} \frac{W}{m \cdot K}$

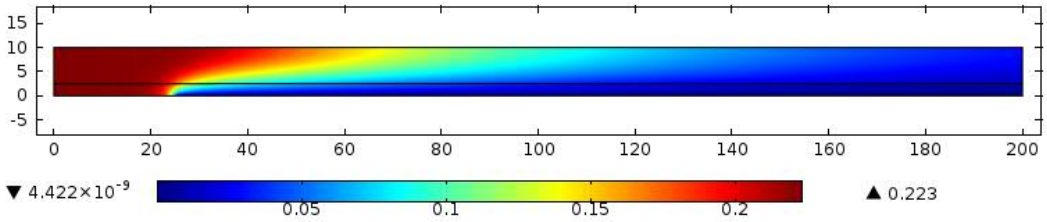

(c) $k = 0.015 \frac{W}{m \cdot K}$

Figure 4.4: (a) At low flow rates heat loss to the inlet boundary is significant because the conductive time scale is sufficiently shorter than the convective time scale. The variation from artificially low conduction to artificially high serves to highlight the effects. Mole fraction is plotted for the top boundary of the channel. (b) and (c) show mole fraction of H_2O_2 for $k = 1.0 \times 10^{-4}$ and $k = 1.5 \times 10^{-2}$respectively.

4.2.1 Mass Diffusion

It has been identified that mass diffusion plays a significant role in the behavior of this model. Due to the lack of turbulent flow mixing inherent to the micro-cale, mass diffusion is the sole mode of cross-stream mass transfer. Fick's law with simple binary diffusion coefficients does not accurately predict the rate of mass transfer multi species model because readily available diffusion coefficients are only valid for diffusion in air. For a very dilute mixture in air these values give a reasonable approximation because each species is relatively unaffected by the others. In a concentrated mixture binary diffusion coefficients for H_2O_2, H_2O, and O_2 (each in air) do not account for the interaction between species. In this model the solvent is a water vapor-oxygen mixture rather than air. To accurately predict mass diffusion a ternary model is needed. Cussler[8] explains that diffusion is often assumed to be binary with one dilute solute in one solvent when this is often not the case. This is done because calculating multicomponent concentrated diffusion is much more complicated. Multicomponent effects are negligible for dilute species, but can be significant in concentrated mixtures. Cussler provides a system of equations to determine diffusion coefficients in ternary systems. The ternary model can be mathematically converted to a binary problem, solved, and then the solution can be applied to the or initial ternary problem. The conversion process utilizes a diffusion coefficient matrix whose eigenvalues represent psusedo-binary diffusion coefficients. A table of diffusion coefficients shows that in concentrated solutions the ternary values are *typically less than 10% of their binary counterparts and can be as much as 2 orders of magnitude less.* Unfortunately the empirical diffusion data needed is not available for the mixture being considered. Therefore, in this model a *binary diffusion model is utilized with the solvent approximated as a mixture of water vapor and diatomic oxygen.* For this approximation

a reasonable diffusion coefficient for H_2O_2 (solute) in the solvent mixture must be estimated. For lack of empirical data, a parametric study has been completed to determine an order of magnitude approximation for this coefficient. While this approximation falls short of providing an exact critical length due to uncertainty, it does provide a means to optimize the configuration (i.e. pillar size and spacing).

Here the diffusion coefficient has been studied for values ranging from those typical for binary diffusion of hydrogen peroxide vapor through air ($\approx 1.88\times10^{-5}\frac{m^2}{s}$) to values typical of diatomic gasses through water ($\approx 2.5\times10^{-9}\frac{m^2}{s}$). A value that most closely reflects the expected length scale is sought. Figure 4.5 is a plot of concentration verse downstream distance at the centerline of a rectangular channel with an inlet velocity of 1.0 m/s. At this flow rate, decomposition is almost instantaneous for values at the low end of the range. Work by Bonifacio shows that this does not accurately represent the length scale expected [4]. Experimental results also imply that the length scale is likely much longer. From a practical approach, this high rate of diffusion means that once vaporized the decomposition is not effected by geometry. For the present study of geometric effects the contrary assumption has been made. For this reason values for $D < 10^{-}7m^2/s$ will not be considered. This plot also shows that values toward the upper end of the range significantly increase the computational domain needed to observe complete decomposition. A larger domain increases computational demands above what is available and does not produce more valuable information or provide insight into the dynamics of the flow. It equates to a stretching effect, but does not change the shape of gradients. For this reason a value of $1\times10^{-}7\ m^2/s$ was chosen for this study. While this cannot lead to a reliable determination of the critical length scale, it will serve to study geometric considerations. Critical length can be easily studied experimentally by creating a domain sufficiently longer then estimated and observing the flow. Geometric permutations would require the prototyping of several

reactors and the costs associated with doing so. Numerical studies are currently inadequate to predict length, but can determine optimal spacing.

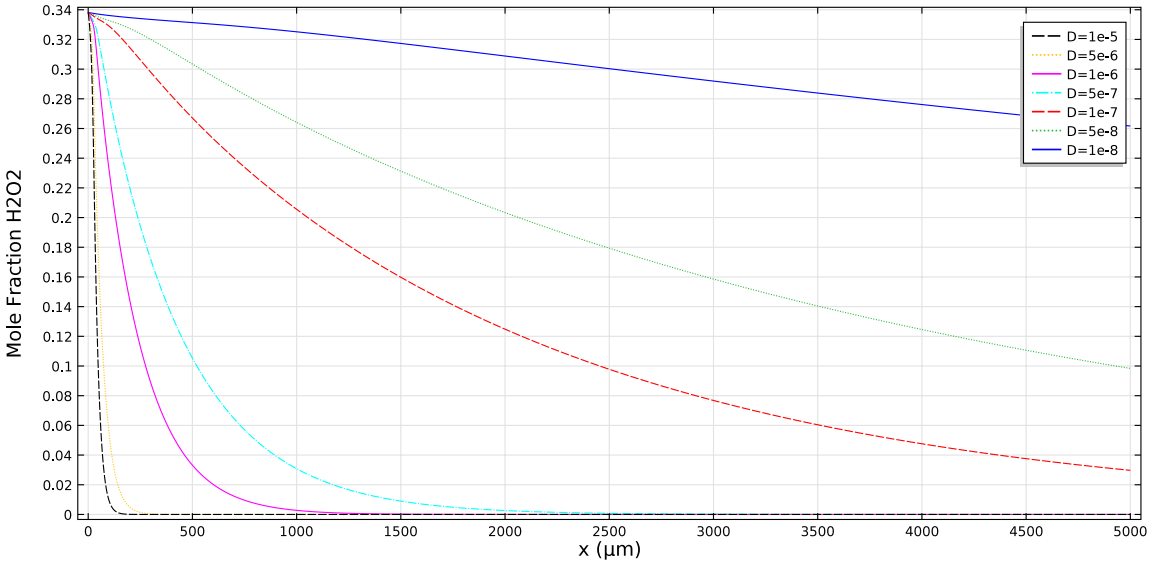

Figure 4.5: Plotted is concentration at the centerline of a 20 μm with an inlet velocity of 1 m/s for the range of diffusion coefficients considered. Between $D = 5 \times 10^{-7} m/s$ and $D = 1 \times 10^{-7} m/s$ a transition is observed.

4.2.2 Kinetic Parameters

In the 0D solution for the Arrhenius equation the effects of the exponential pre-factor and activation energy are significant. A 2D model introduces mass and energy transfer which complicate evaluation. The decomposition rate may be limited by these modes rather than the reaction rate. The exponential prefactor was modeled for a large range of values in the literature from 10^6 to 10^{11} as in the 0D model. Very little effect is observed on this large range. Plotting mole fraction along the centerline of the channel shows essentially no change for the range studied, see Figure 4.6. A similar examination of reasonable values for activation energy showed no change for values ranging from 30 kJ/mol to 60 kJ/mol as shown in Figure 4.7 From this it can be

deduced that the reaction rate is not the limiting factor and has very little effect on critical length. It also implies that residence time is not important on this scale. More precisely, decomposition length is determined by mass diffusion rather than surface interactions.

4.2.3 Inlet Velocity

For a fixed cross section, thrust is proportional in inlet velocity. To increase thrust inlet velocity can be increased. In chapter 2 this relationship is expressed in detail. Here the effect of inlet velocity on decomposition length is studied. One would expect decomposition length to be proportional to velocity. Figure 4.8 plots centerline concentration verse inlet velocity. From this plot it is evident that decomposition length scales with velocity as would be expected.

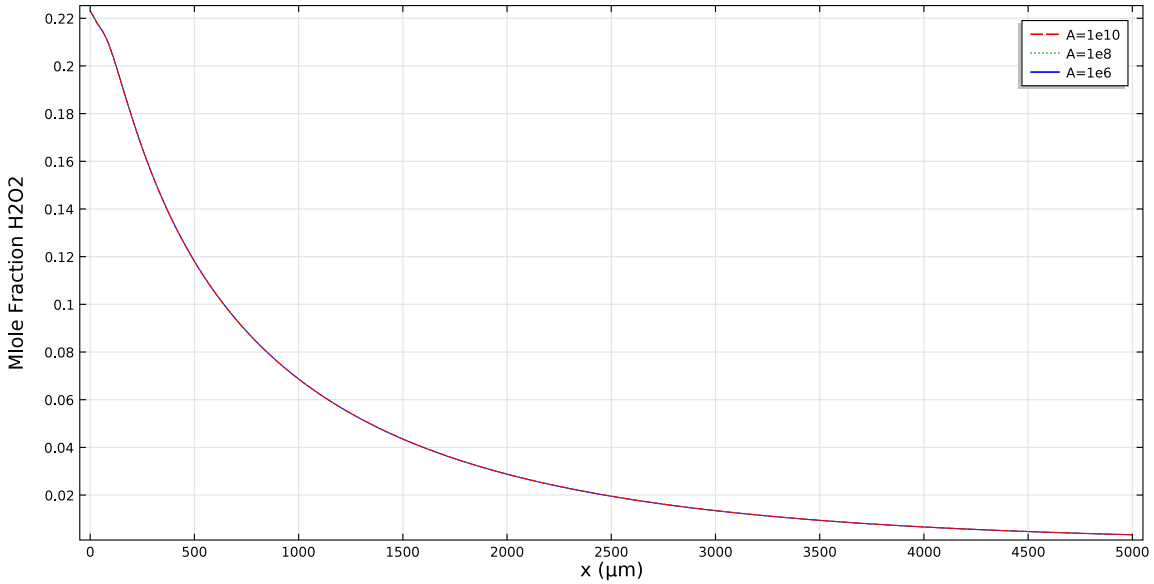

Figure 4.6: Kinetic parameters do not play a meaningful role in the decomposition of hydrogen peroxide in a micro channel. This is shown with a parametric study of the exponential prefactor from 10^6 to 10^{11}. Over this range there is no meaningful variation in centerline mole fraction.

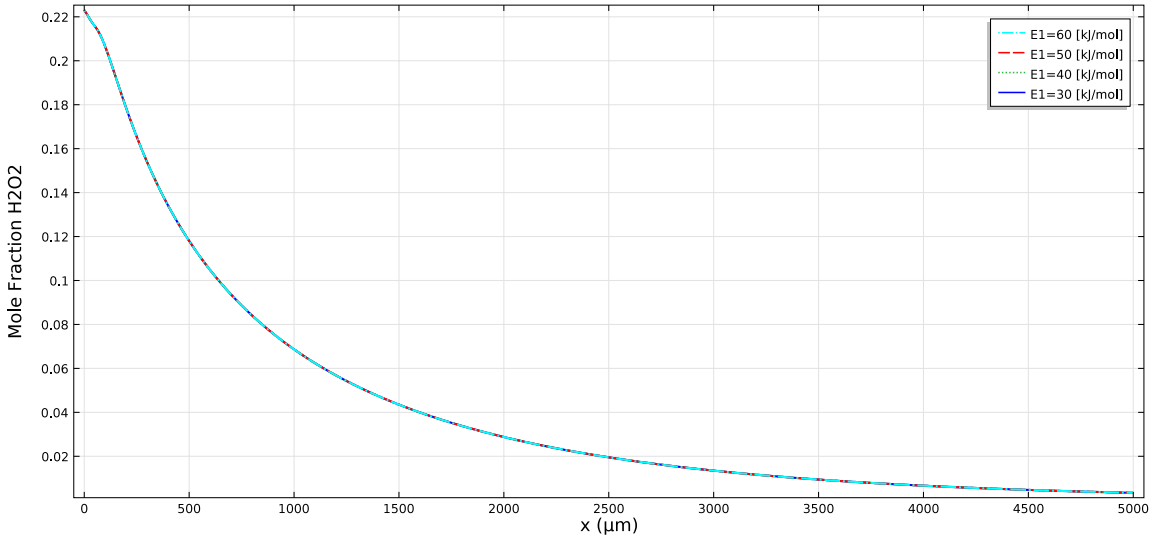

Figure 4.7: Mole fraction along the centerline does not change for the range of activation energies studied. When mole fraction is plotted along the center of a slender channel ($d = 20\ \mu$) there is no discernible effect of activation energy on this scale. It can be deduced that mass diffusion is the limiting factor rather than chemical kinetics.

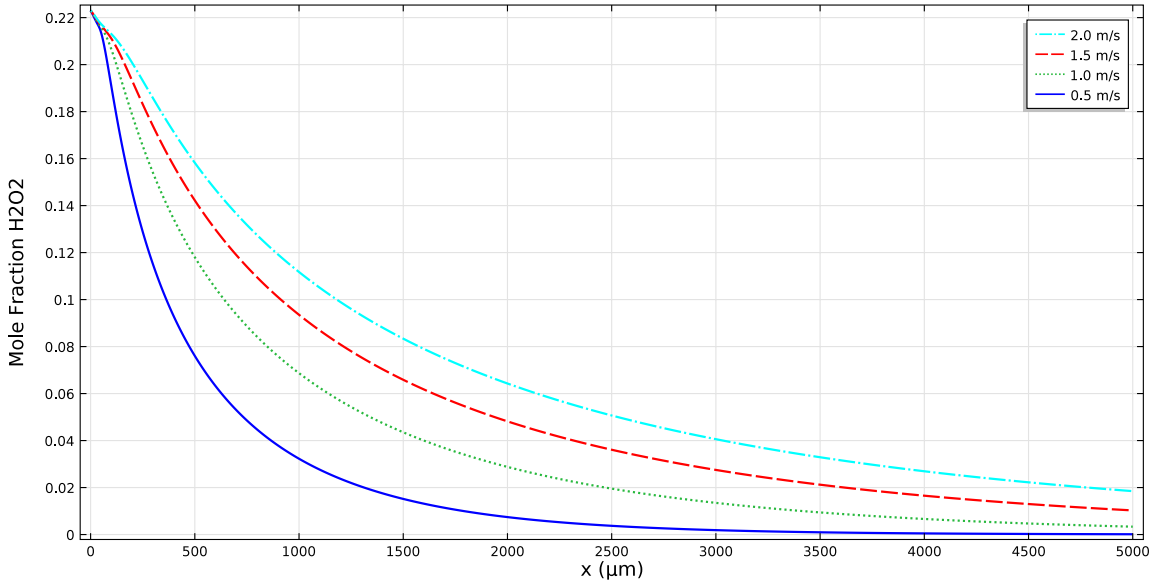

(a)

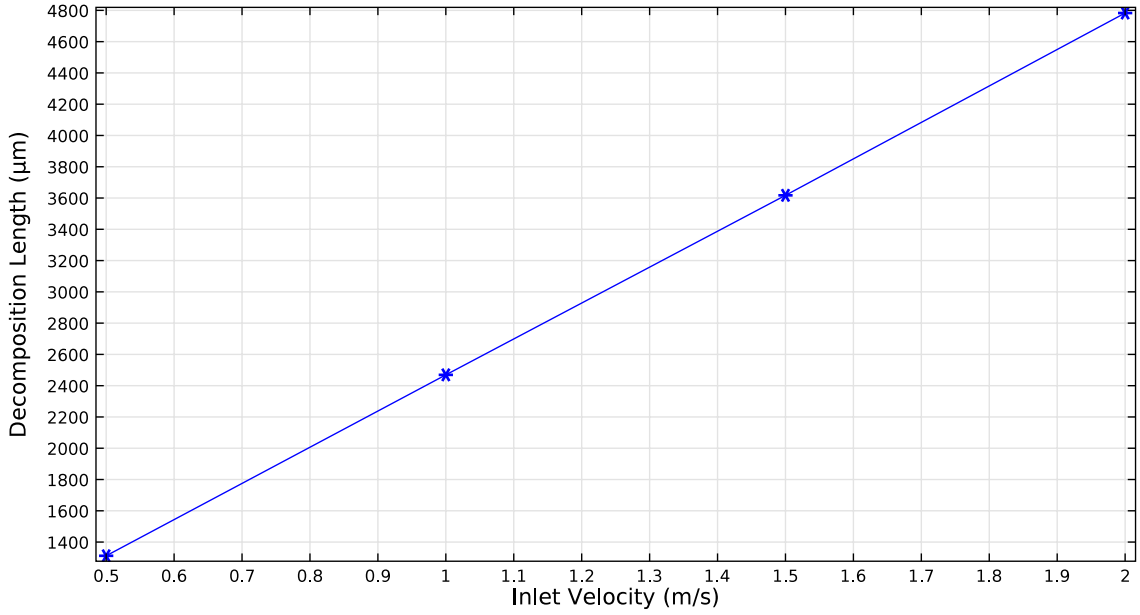

(b)

Figure 4.8: (a)Centerline concentration plotted for a 20 μm rectangular channel by interpolation provides estimated that doubling inlet velocity results in a two time longer decomposition length. (b)The linear relationship between inlet velocity and critical length is show here. Complete decomposition was determined when the mole fraction of H_2O_2 fell below 0.02.

4.3 2D Model of Catalytic Pillar Geometry

After model parameters were verified using the simplified wall model, the original pillar configuration was considered. The main result pursued in this investigation was the geometric optimization, namely the pillar size and spacing. To this end a parametric study was conducted to determine where critical length was minimized and flow characteristics were maximized. For a fixed channel width of 1103 μm, a subregion size 1/26th of the total channel was fixed at 42.43 μm. The layout is constrained so that catty-corner pillar walls are collinear. This caused the diagonal distance comprised of a pillar length plus the pillar spacing to be fixed at 60 μm. The driving parameter was pillar spacing and pillar sizing was determined from this relationship. The standard comprised of 40 μm pillars with 20 μm spacing was used in all cases except when in the geometric optimization study. Prior to the geometric optimization material properties and kinetic parameters were investigated.

4.3.1 Mass Diffusion

The dominance of mass diffusion as a controlling factor in the decomposition of hydrogen peroxide justifies taking a second look at the diffusion in the pillar configuration. The same bounds are used for this investigation as were in the straight channel, namely $1.0 \times 10^{-5} \frac{m^2}{s}$ to $1 \times 10^{-9} \frac{m^2}{s}$. Surface maps of mole fraction for a range of diffusion coefficients (Figure 4.9) illustrate the role of mass diffusion, but do not provide a useful quantitative comparison. For this relationship refer to the corresponding study of the straight channel which showed the difference in length scale. For parametric studies of velocity and pillar spacing the median value of $1.0^{-}7$ was used.

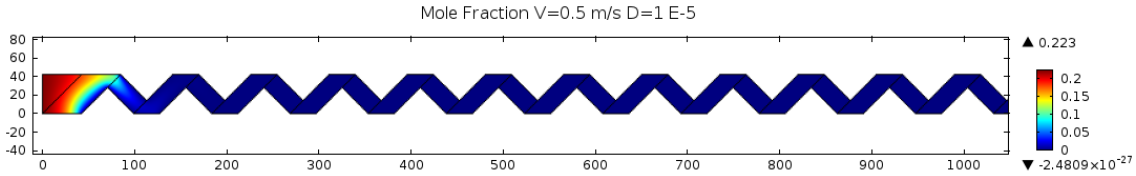

(a)

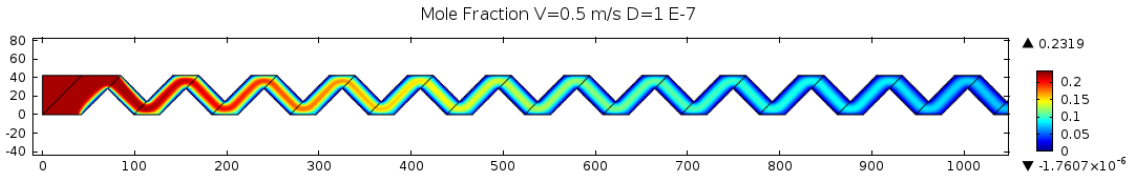

(b)

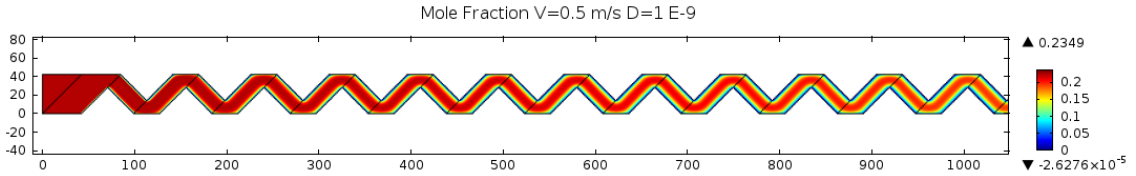

(c)

Figure 4.9: Surface maps of mole fraction provide a visual representation of the drastic impact of diffusion on critical length ranging from immeasurably short (1 $\times 10^{-5} m^2/s$) to very long(1 $\times 10^{-9} m^2/s$). For the purposes of this project a median value of 1 $\times 10^{-7} m^2/s$ is used. In future work, diffusion should be revisited for a more accurate determination. For a worst case approach, values at the high end of the range should be used.

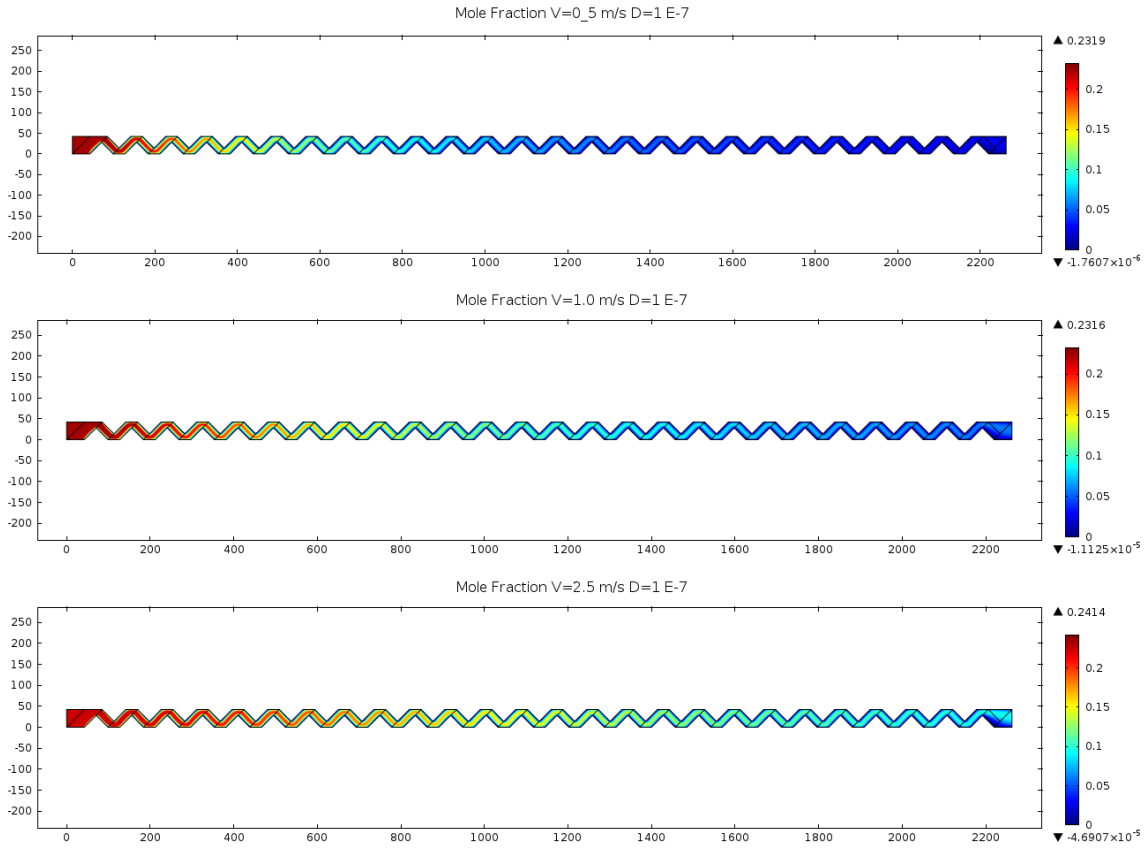

Figure 4.10: Surface plots of concentration demonstrate the dependance of critical length on inlet velocity. Due to the serpentine nature of the flow it is difficult to determine a location for complete decomposition. For a more quantatative relationship refer to the reactive wall model.

4.3.2 Pillar Size and Spacing

It is intuitive that by reducing pillar spacing, critical length is drastically decreased. It is equally intuitive that by restricting the flow pressure drop along the channel is increased. For this mass flow driven model, inlet pressure is determined computationally from the inlet velocity, the outlet pressure, and viscous loses. Here inlet pressure is monitored to better understand at what point the flow has been restricted further than design parameters permit. This threshold is crossed for a pillar spacing of less than 10 μm, which is selected as the cutoff point for spacing reduction. For lower values the flow becomes restricted and a greatly increased reservoir pressure would be needed to maintain the prescribed flow rate. With the knowledge that diffusion is the rate limiting processes it is not surprising that reduction in pillar spacing reduces decomposition length even though the flow is accelerated. Figure 4.12(b) shows that when pillars are spaced 40 μm apart only about half of the hydrogen peroxide is decomposed in the domain while the exhaust the 10 μm spacing is comprised of approximately only 1% HTP. A diminishing return is observed for smaller spacing. From this analysis it is concluded that in the vapor region of the flow channels as narrow as 10 μm are warranted for reduced critical length.

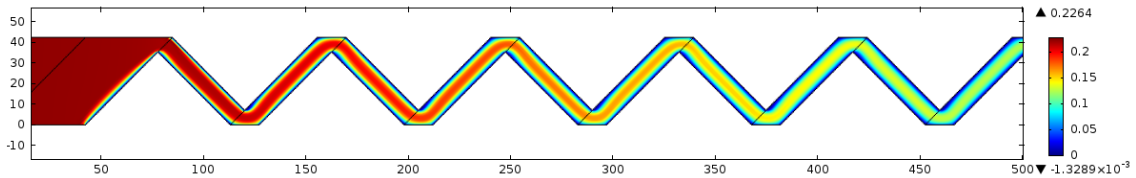

(a)

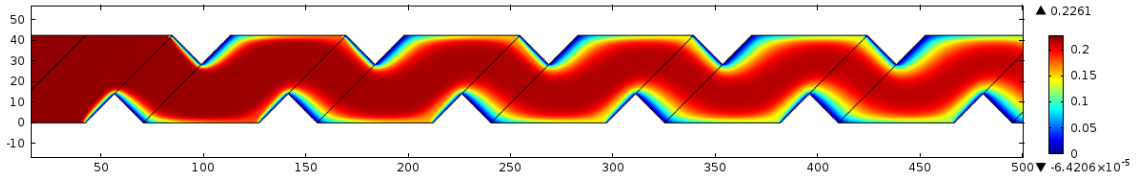

(b)

Figure 4.11: Surface maps of mole fraction are compared for an arrangement with 10 μm pillar spacing (a) and 40 μm spacing (b). It can be observed that decomposition occurs much further downstream when pillar spacing is increased.

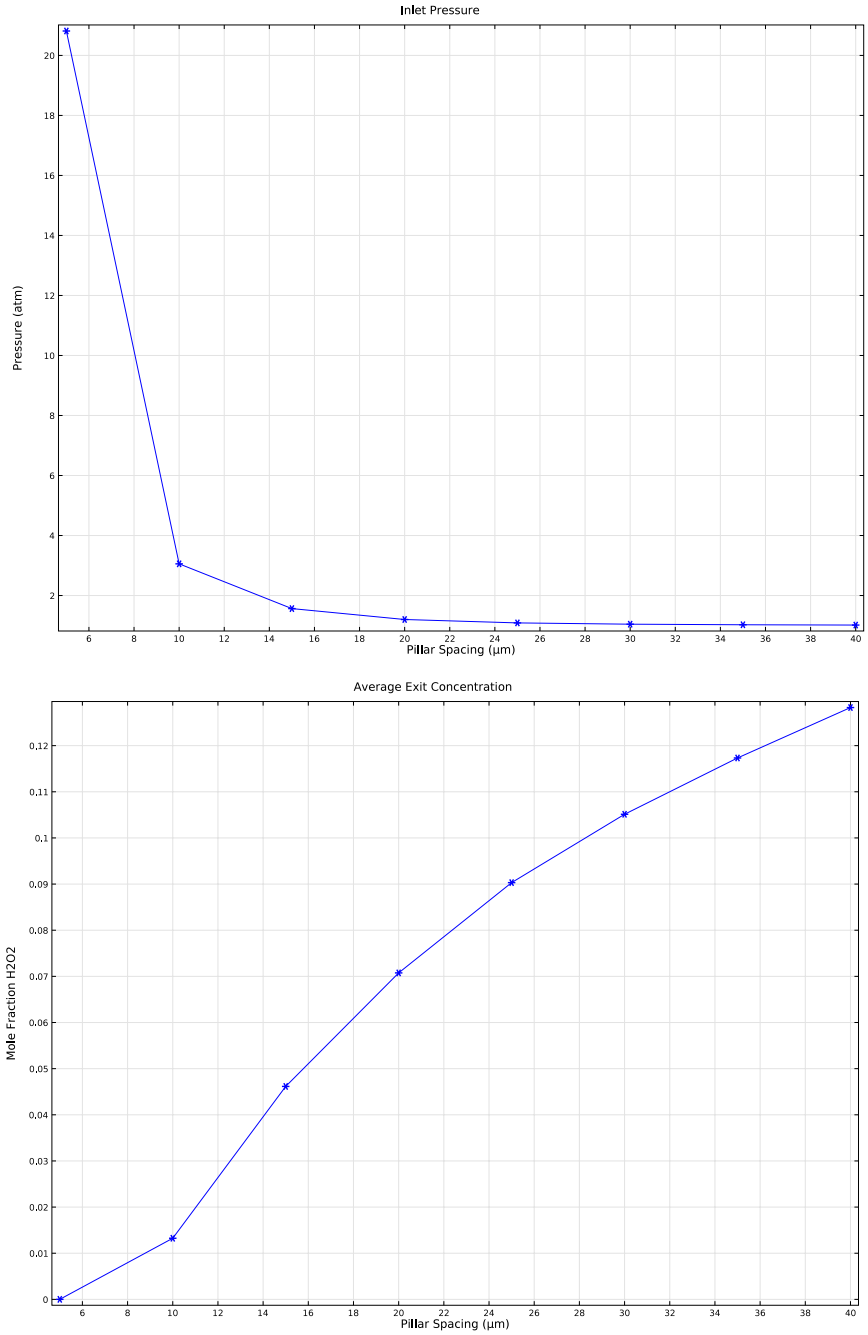

Figure 4.12: Average inlet pressure was plotted to assess the effects of the flow constriction. For this study the inlet velocity is fixed at 2.5 m/s. It can be seen that for pillar spacing less than 10 μm inlet pressure is drastically increased to values much larger than design constraints. The concentration of hydrogen peroxide was average over the exit plane and plotted against pillar spacing. Here for pillar spacing greater than 10 μm, decomposition decays exponentially.

Chapter 5

Experimental Results

The experimental goals are three-fold. The primary goal was to prove that ruthenium oxide (RuO_2) nano ods can catalyze the decomposition of hydrogen peroxide HTP. The secondary goal was to quantify any decomposition that was observed. This was to been done using visual inspection aided by high speed photography, and monitoring temperature variation using thermal imagery. To this end experimental results are shown for mesoscale and microscale experimental configurations. Initial experiments on mesoscale showed that RuO_2 could perform as a catalyst over repeated runs and served as practical experience handling rocket grade hydrogen peroxide. High temperatures caused fittings to fail, resulting in device failure. Figure 5.1 shows a glass catalytic chamber with a conical nozzle at the outlet. Steam can be seen exiting the nozzle. This prototype functioned well for several seconds before the nozzle melted and clogged. This forced a change to an all metal prototype. The drawback of a metal section is the inability to observe the flow. This leaves the steam exiting the channel as the only indication of decomposition. In addition to high temperatures, significant pressure build-ups were observed, which resulted in two failure types. The first type were physical failures including plastic fittings and syringes. High pressure was also

responsible for stalling the syringe pump. Second, significant back flow was noted. This is a significant problem because it can carry contaminates or potential catalyst upstream making the device uncontrollable and affect thrust production. This could possibly be addressed by adding a pressure reduction between the syringe and the reactor. It is possible that clogging cannot be avoided with the use of a simple powder. When moving to the micro-scale, replacing ruthenium powder with nanorods removes this complication.

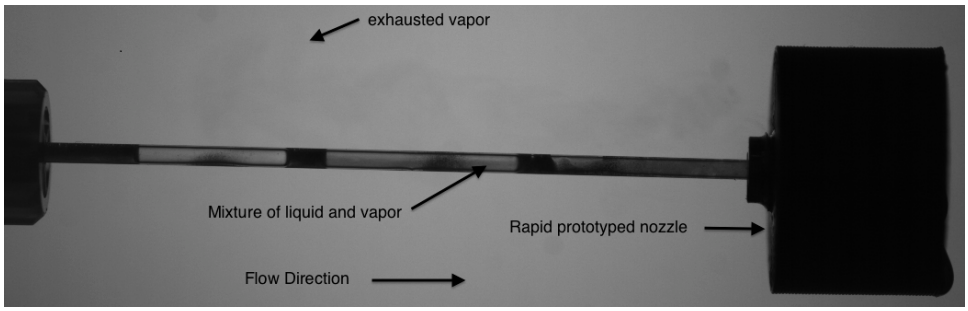

Figure 5.1: The mesoscale thruster achieved some of the original design goals of creating fully vaporized products. Significant back pressure resulted in vapor flowing upstream. Clogging and melting of the rapid prototyped conical nozzle forced a transition to metal components.

5.1 MEMS reactor

Prior to testing in a sealed micro-channel, the reactivity of nano rods was tested by pipetting $1\mu L$ droplets of HTP onto substrates with nanorods. The first sample was a flat surface with nanorods. Figure 5.2(a) shows very high activity. The photograph was taken normal to the surface. Small gas bubbles can be seen forming on the surface. Bubbles then detach from the surface and begin to rise coalescing into larger bubbles before reaching the surface. A magnified image better depicts the coalescence. High speed photography taken at 300 frames per second distinctly shows the high rate of

bubble formation. A control sample was tested for comparison. The control sample was a clean silicon substrate without nanorods. Figure 5.4 shows that no activity is seen thus proving that the nanorods are responsible for the gas generation. A second sample was tested. This sample consisted of nanorods grown on pillars in a micro-channel. Again a $1\mu L$ droplet was placed on top of the channel. The bubble wicked into the channel and gas generation was observed. From these samples it was concluded that nanorods are capable of acting as a catalyst for the decomposition.

Once the samples were complete, each was inspected for defects. Some samples were found to have imperfections; which were typically blockages created by either incomplete etching or breakage (figure 5.5). In some cases pieces of the wall would separate and become lodged in the flow. It is assumed that this was the result of a combination of handling and contamination. With a proper clean room and refined manufacturing process this would likely be minimized.

The first channel to be tested was the smallest configuration (Figure 5.7). The square pillars are 40 μm on each side and the channels are 20 μm across. This represents a small lengthwise subsection of the NASA Goddard geometry. At the end of the channel are bubbles of gas that have been generated. In this image the nanorod covered pillar array is approximately 2 mm, which for the flow conditions is clearly insufficient for full decomposition but proves the feasibility nicely. Comparisons between this test and those performed by GSFC show many similarities and stand to confirm that while the use of RuO_2 nanorods is sound, the geometric design needs work. Video taken during the experiment shows asymmetric flow patterns as well as inconsistent velocity. It appears that flow is not preferential to a particular channel until a sufficiently large gas bubble is generated. This bubble subsequently becomes lodged in one channel making the other channel preferential. Flow remains diverted until the flow condition changes in a way that again makes that channel preferential.

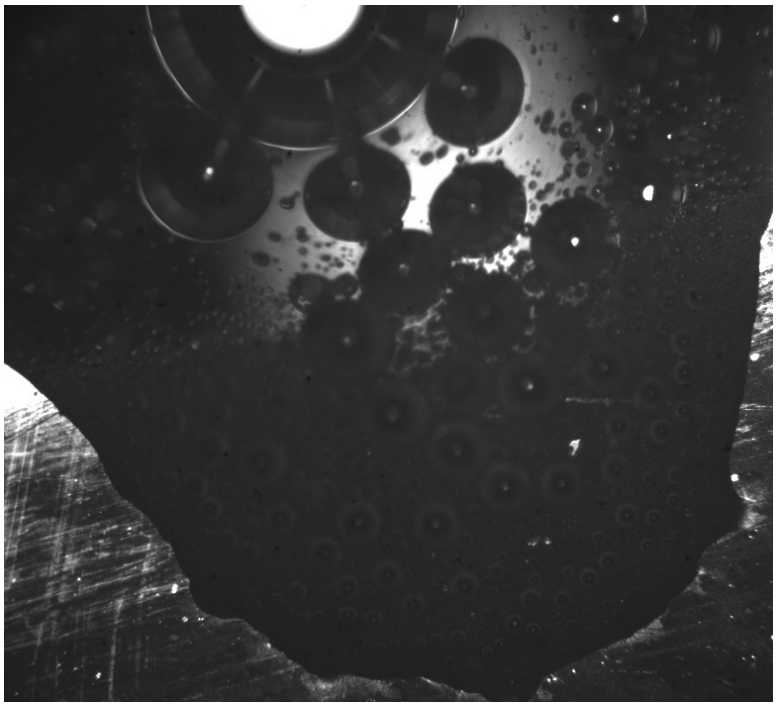

(a)

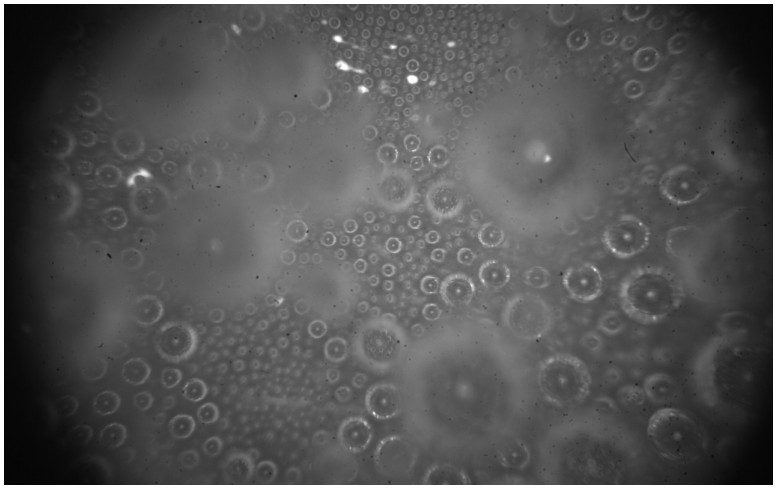

(b)

Figure 5.2: These frames taken at 5x (a) and 20x magnification (b) show the reaction caused by the ruthenium oxide nanorods. In this demonstration $1\mu L$ of 90% HTP was placed on a nanorod covered substrate. The gas generated shows the high level of activity that was observed.

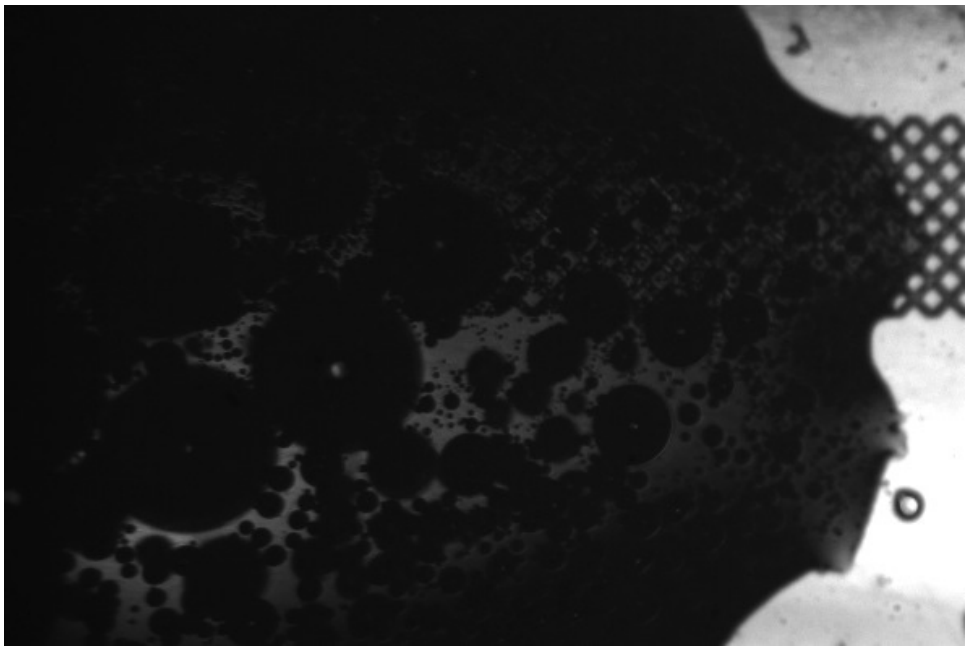

(a)

(b)

Figure 5.3: These pictures were taken at 5x (a) and 20x magnification (b). $1\mu L$ of 90% HTP was placed on top of nanorod covered pillars and allowed to wick into the channel. While this surface does not appear to be as reactive as the flat wall, gas is generated at the pillar walls. If decomposition is seen in an open channel with a relatively large quantity of liquid, it should follow that it will be observed in a closed channel where the surface to volume ratio will be much higher.

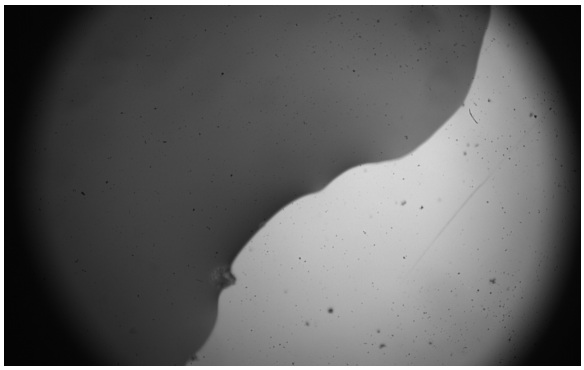

Figure 5.4: This control sample was photographed to show that the silicon substrate does not catalyze hydrogen peroxide. When compared to the reactive samples, one can readily see the activity caused by nanorods.

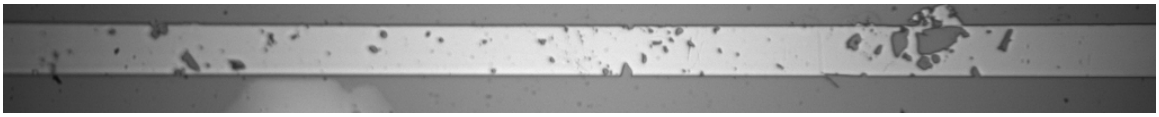

Figure 5.5: This picture was taken during a pre-experiment inspection and shows a flaw that was detected. Similar flaws were occasionally detected and show that careful manufacturing will be necessary to produce useable thruster with regularity.

.. 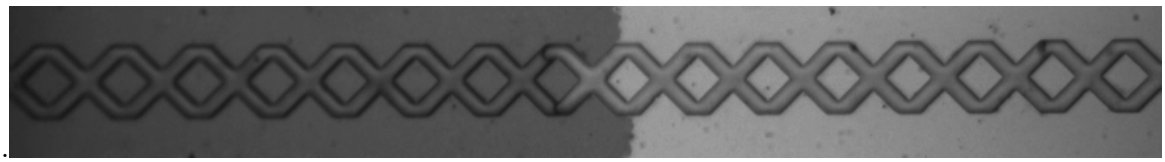

Figure 5.6: In some cases wicking was observed between the silicon substrate and the pyrex cover sheet indicating imperfect boding. Here the liquid outside of the channel progresses forward ahead of the meniscus in the channel.

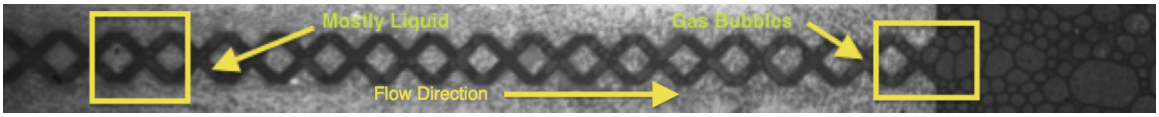

Figure 5.7: Pictured is one row of square pillars with $40\mu m$ sides with 20μm channels carrying flow from left to right. The inlet is 90% H_2O_2 liquid at room temperature. To the far right of the image gas bubbles generated by decomposition are visible. The vapor fraction increases from left to right signaling the continued decomposition of the flow. These match closely with results found by Hitt et al.[11] for the full NASA Goddard thruster and are encouraging for the use of nanorods as a catalyst.

In the wider channel, tracking bubble patterns becomes more complicated as there are several available routes. Video taken of configuration (d) have been analyzed in an attempt to qualify path choice. Here it becomes more evident that the path is random and is determined by surface tension effects. For this particular experiment the channel was held vertically to facilitate thermal imaging. The high speed video camera was placed horizontal viewing the front of the channel and the thermal camera was placed behind the silicon substrate viewing the back of the sample. This was done because pyrex is opaque to infrared light, while silicon is transparent. Unfortunately, no variation in temperature was observed by the camera.

5.1.1 Additional Visualizations Challenges

The reactor operation appears to deteriorate in time. After several minutes of operation gas generation diminishes significantly. This could be caused by several factors including physical deterioration of the nanorods. Unfortunately once the channels have been sealed a SEM can not be used to inspect the nanorods. Nanorods only become visible at about 3,000x. The highest magnification available after the channel has been sealed is 50x, which does not provide any information about the nanorods physical condition. It was hypothesized that a liquid water layer formed on the

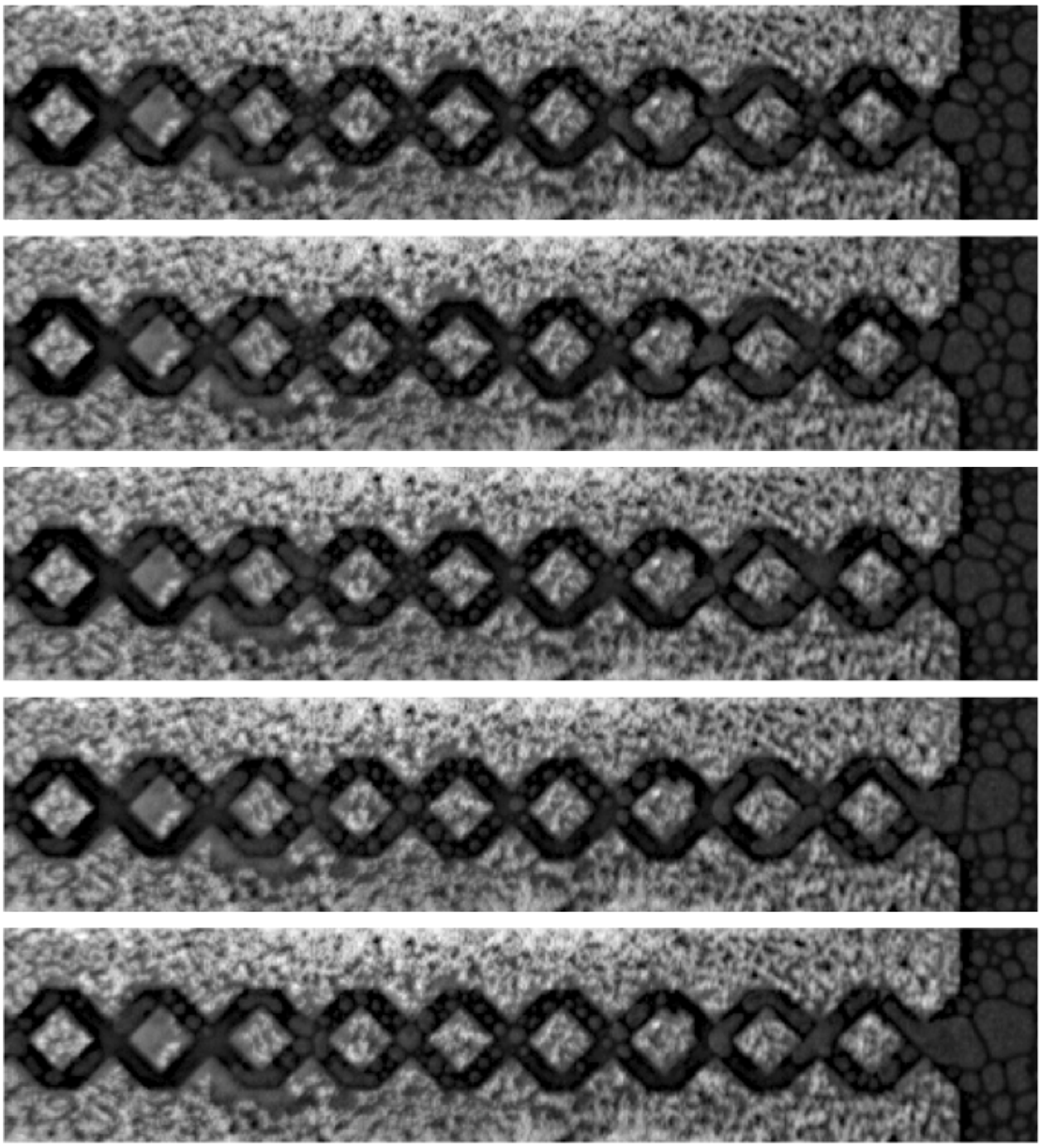

Figure 5.8: The image sequence shows a small glimpse into flow patterns created by decomposition. Video provides a more qualitative view of clogging that takes place. By tracking specific bubbles through the flow it can be seen that with no blockage, gas bubbles tend to remain in the same horizontal subset of the domain. When a larger bubble becomes trapped it essentially blocks that path diverting the flow. The flow is from left to right.

nanorods, which prevented peroxide from contacting the surface. To test this theory, a channel was placed in a vacuum chamber to dry. Once the channel was dry, the experiment was repeated. This showed very similar startup behavior to the first time the channel was used. This suggested that there was no physical deterioration of the nanorods and supports the theory of the formation of a water boundary layer.

5.2 Heat Transfer

An engineering analysis of heat transfer was completed to explain why greater vaporization was not witnessed during the experiments. The pillars were modeled as fins. The base was considered, but the walls were not. For this analysis several simplifying assumptions were made. The fluid was considered to be liquid water at 373 K. The fluid velocity was determined from a gas velocity of 1 m/s and density of 0.58 kg/m^3 using the relationship $\dot{m} = \rho v A = const$. The Reynolds number was found to be 0.12 for liquid water ($\mu = 279 \times 10^{-6}\ Ns/m^2$) and 2.8 for steam ($\mu = 12.0 \times 10^{-6}\ Ns/m^2$), based on the length dimension D being the length of the diagonal of a pillar, 56.6 μm.

$$Re_D = \frac{\rho V D}{\mu} \tag{5.1}$$

The convection coefficient $\bar{h}$ was then estimated by treating the system as an external form around the pillars. Using the correlation equations for noncircular cylinders in a cross flow from Incropera et al.[12]:

$$\bar{N}u_D \equiv \frac{\bar{h}D}{k} = CRe_D^m Pr^{1/3} \tag{5.2}$$

where C =0.246 and m=0.588 for a diamond cross section. $\bar{N}u_D$, Pr and k are the Nusselt number, Prandtl number, and thermal conductivity respectively. Solving for the convection coefficient results in $h = 1025\ W/m \cdot K$. Typically on the macro-scale

correlations for a staggered array would be appropriate for this geometry. These correlations attempt to account for interactions between pillars and to quantity flow separation. However, on the micro-scale the Reynolds numbers are far lower than on the macro-scale. No flow separation is observed numerically or experimentally. It can be assumed that there is no meaningful interaction between adjacent pillars. For this reason only a single pillar was considered. Once an estimate for h was determined the heat transfer rate for a fin was calculated. Assuming a uniform cross section, heat transfer in a fin can be described by Equation (5.3), where P is the fin parameter, A_c is the cross sectional area, and T_∞ is the fluid temperature. The excess temperature Θ is introduced and its derivative is equal to the derivative of $T(x)$ because the fluid temperature is assumed to be constant.

$$\frac{d^2T}{dx^2} - \frac{hP}{kA_c}\Theta(x) = 0 \tag{5.3}$$

$$\Theta(x) = T(x) - T_\infty \tag{5.4}$$

$$\frac{d\Theta}{dx} = \frac{dT}{dx} \tag{5.5}$$

$$\frac{d^2\Theta}{dx^2} - m^2\theta = 0 \tag{5.6}$$

Substituting (5.5) into (5.3) and defining $m^2 \equiv \frac{hP}{kA_c}$, the solution of the linear homogenous second-order ODE can be given by the general form:

$$\Theta(x) = C_1 e^{mx} + C_2 e^{-mx} \tag{5.7}$$

Where C_1 and C_2 are determined from the boundary conditions, which were a prescribed a temperature at the fin base and an assumed adiabatic fin tip. The top of the fin was considered adiabatic because the thermal conductivity of the pyrex cover slide is far lower than that of the silicon substrate. Solving for the constants of integration

results in a solution for the temperature distribution, (5.9).

$$\Theta(0) = T_b - T_\infty \qquad \frac{d\Theta}{dx}(L) = 0 \tag{5.8}$$

$$\frac{\Theta}{\Theta_b} = \frac{cosh\ m(L-x)}{cosh\ mL} \tag{5.9}$$

Applying Fourier's law at the bases allows for the heat transfer rate for the fin to be determined.

$$q_f = q_b = -kA_c \frac{d\Theta}{dx}|_{x=0} \tag{5.10}$$

Substituting (5.9) and solving results in (5.11), where $M = \sqrt{hPkA_c}\Theta_b$.

$$q_r = M\ tanh\ mL \tag{5.11}$$

Entering values for M and m result in a heat transfer of approximatly 2 mW per pillar. The heat generated by the chemical reaction is estimated by $Q = kC_{H_2O_2} \cdot 98[kJ/mol]$ where k is determined by the Arrhenius equation. Multiplying the heat generated per unit area by the surface area of one pillar will provide a comparison between the heat added at the surface and the heat removed by conduction. The heat per pillar was determined to be approximately 20 mW or ten times larger then the heat removed. For this application these values are sufficiently close enough in scale to determine that the heat removed from the fluid by conduction is significant. An efficiency calculation for a single fin resulted in $\epsilon \approx 10$ when compared to a plain wall. The efficiency of the fins combined with the high conductivity of silicon result in significant heat removal from the flow. This cooling adversely affects the reaction rate which is exponential in temperature and may drastically diminish performance. This could be mitigated by reducing the size of the silicon substrate as much as possible and surrounding it in an insulating material (figure 5.9(a), or it could be exploited to preheat the hydrogen peroxide before it enters the catalyst bed (figure

5.9(b)). Preheating the hydrogen peroxide before it enters the reactor has several effects. Surface tension decreased with temperature, reducing clogging. Also, the reaction rate is exponential with temperature.

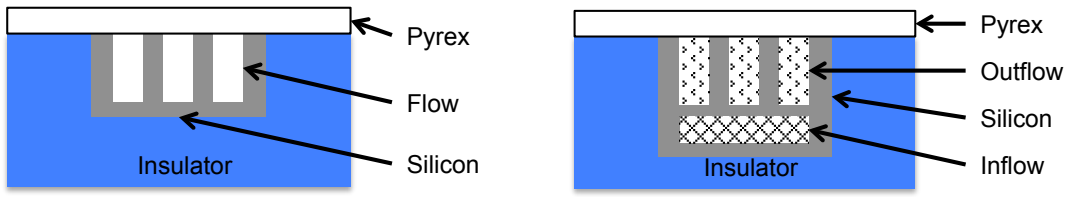

(a) (b)

Figure 5.9: Heat loss through the substrate may be significant enough to quench vaporization. To this end schemes to reduce heat loss should be explore. This simple illustration shows two general idea. (a) To reduce heat loss the very conductive silicon substrate should be wrapped in an insulating material. (b) The conductivity of silicon could also be exploited to preheat the hydrogen peroxide before it enters the reactor. Preheating would have several benefits including reduced surface tension and increased reaction rate. In the sketch the inflow is directed out of plane and the outflow is directed into the plane of the picture.

5.3 Microslug

In an effort to determine the role, if any, surface tension plays in channel clogging a multi-phase model was employed. In this level-set model gas bubbles are generated at a cross junction and passed through an array of pillars with a $10\mu m$ spacing. The overall channel width is $50\mu m$. The three inlets have a set velocity 0.4 m/s and the outlet is gage pressure. The top and bottom inlets are water, while the left-hand inlet is air. An interested reader can reference work by McDevitt et al. [17] [18] for more model details. The gas bubbles separated by fluid are then passed through the pillar array. This model ignores that symmetry boundaries present in the larger geometry and therefore does not allow for alternate paths. The goal of this study

is to isolate surface tension form other effects. The level-set function varies from 0 (representing air in blue) to 1(representing water in red). The 0.5 iso-contour reprints the interface between the fluids. Figure 5.10 shows that as gas bubbles pass through the pillars they are deformed. The gas adheres to the surface of the last pillar causing the monodisperse flow to transition to a stratified flow.

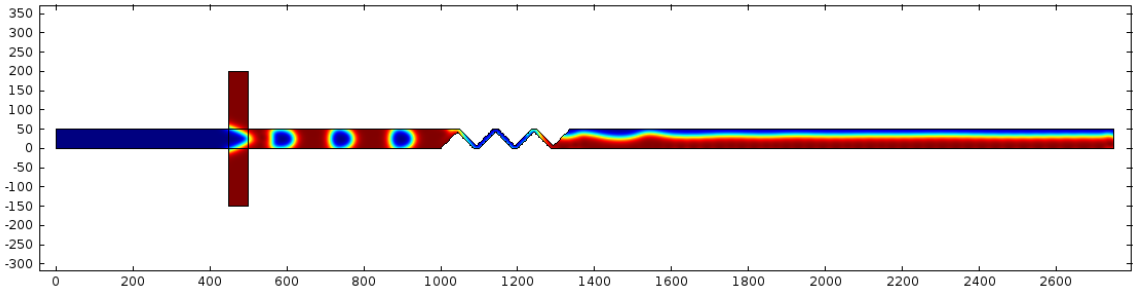

Figure 5.10: A surface plot of volume fraction shows that discrete gas bubbles pass through an array of offset pillars the bubbles adhere to the surface of the last pillar. This causes the flow to separate with the gas at one side of the channel and the fluid at the other. Here blue corresponds with gas and red is liquid.

The adhesion observed at the trailing edge of the pillar array shows the surface tension is likely the driving force causing bubbles to become lodged between adjacent pillars. At the low Reynolds numbers associated with micro fluidics, inertial forces are are dominated by viscous forces. This means that a slight fluctuation in pressure caused by a temporary blockage could divert the flow to a path of less "resistance." This diversion would continue until flow conditions change in favor of the original route causing the bubble to dislodge.

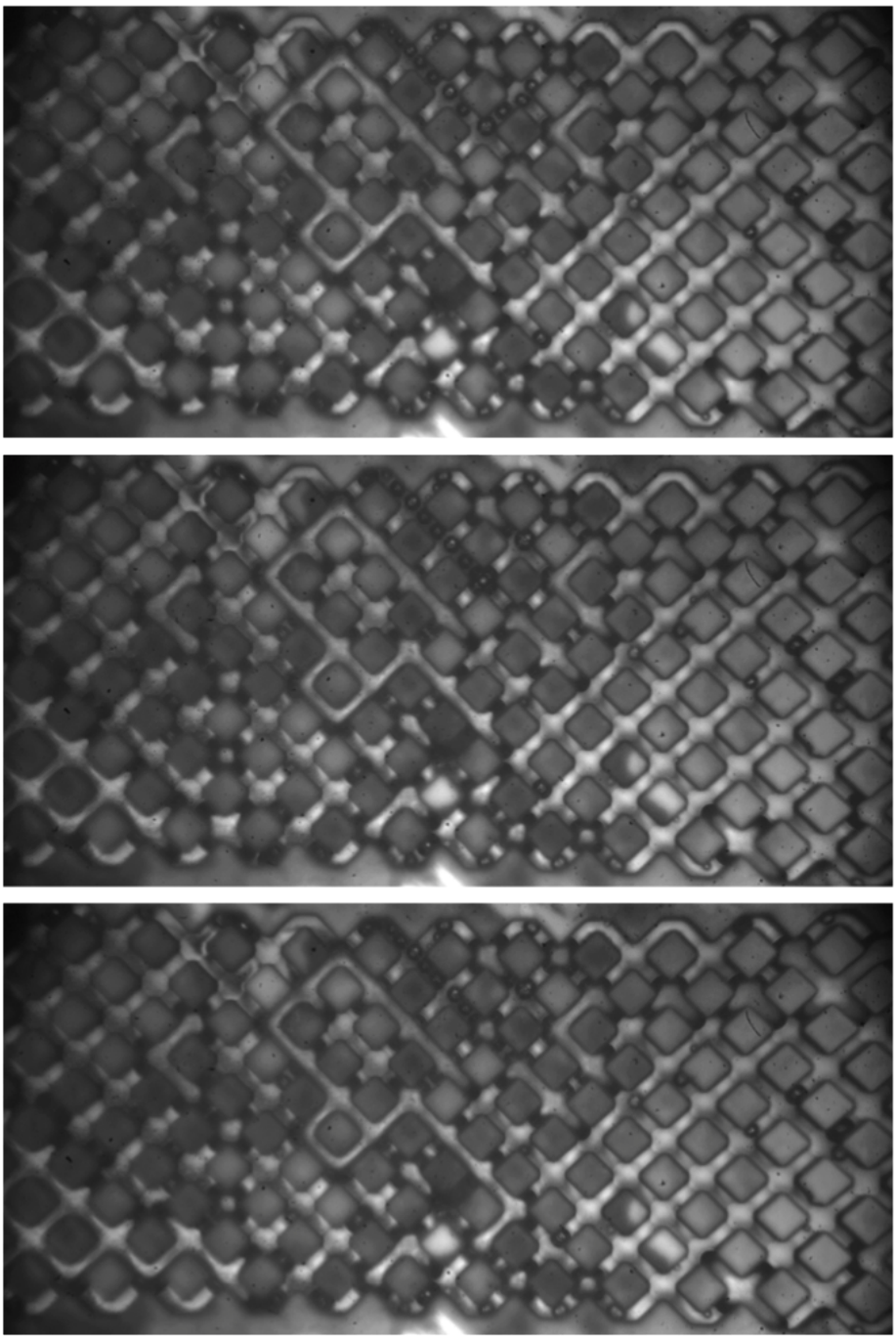

Figure 5.11: This image sequence attempts to characterize the flow patterns observed in the high speed video. In the top center several small gas bubbles can be seen. In the first three frames the bubbles are being pushed backward. This back-flow can be observed periodically as gas bubbles become lodged between adjacent pillar causing tempera try blockages. An injector located upstream of the channel could prevent back flow by regulating temperature. Wider channels would reduce blockages.

Chapter 6

Conclusions

Gas phase numerical models suggest narrow channels on the oder of approximately 10 μm are optimal, while experimental results suggest that wider channel may prevent blockages and allow for a more uniform flow through the array. This discrepancy is most likely explained by multiphase nature of the flow. A design that meets both criteria may be useful. If the flow can be partially preheated surface tension will be reduced, which will mitigate clogging. A two stage design may also be useful. The first stage should be designed with liquid flow in mind. This region should have widening spacing as gas is generated. Once the flow is vaporized it would enter the second stage of the reactor. This region would be comprised of very closely placed pillars as suggested by the computational model.

Further investigation into ternary diffusion models should be pursued to accurately predict gas phase critical decomposition lengths. While kinetic parameters were determined to have little effect, mass diffusion is the driving force. The coarse approximation used here sufficed for geometric optimization, but is insufficient to determine length.

Simple heat transfer calculatiosn show that the high conductivity of silicon may

quench vaporization and reduce the effectivity of the reactor. By trimming the substrate to the smallest reasonable size and coating with an insulating material, conductive heat losses could be reduced. A wider and deeper channel would allow for a larger mass flow rate with an energy addition to the system that mitigates the effect of heat loss. The addition of an injector to reduce pressure for the port to the inlet of the channel will help prevent back-flow. Increasing the exit size may also reduce pressure buildup. For the purpose of prototyping a pillar array several times longer than the NASA Goddard design should be pursued. This will aid in determination of the critical length for a variety of flow rates.

References

[1] Asante, Kofi,"Light Trapping Heteroepitaxial Thin-Flim Photovoltaic," Doctoral Proposal, University of Vermont, August 2011.

[2] Baker, J. et al., LISA: Probing the Universe with Gravitational Waves, Version 1.0, LISA Mission Science Office, http://lisa.jpl.nasa.gov/news.html, January 19, 2007.

[3] Bond, G.C.,"Heterogeneous Catalysis: Principles and Applications" 2nd Ed, Oxford Science Publications, 1987.

[4] Bonifacio, S. and Russo, A., "Modelling Hydrogen Peroxide Decomposition in Monolithic Beds, 3rd International Conference on Green Propellant for Space Propulsion and 9th International Hydrogen Peroxide Propulsion Conference , ESA, 2006.

[5] Cervone, A., Torre, L., d'Agostino, L., Musker, A., Roberts, G., Bramanti, C., and Saccoccia, G.,"Development of Hydrogen Peroxide Monopropellant Rockets", 42nd AIAA/ASME/SAE/ASEE Joint Propulsion Conference, July 10-12 2006, *AIAA 2006-5239*

[6] Chiappetta, L.M., Spadaccini, L.J., Huang, H., Watkins, W., and Crocker, A.M., "Modeling a Hydrogen Peroxide Gas Generator for Rockets" 36th AIAA/AS-

ME/SAE/ASEE Joint Propulsion Conference, Huntsville, Alabama, July 16-19, 2000, *AIAA 2000-3223*

[7] Cross, M., Varhue, W. and Hitt, D.L., "Fabrication of Self-Assembled Catalytic Nanostructures" Encyclopedia of Microfluidics and Nanofluidics, 2008.

[8] Cussler, E.L., "Difusion, Mass Transfer in Fluid Systems". New York, Cambridge University Press, 1997.

[9] Greenfield, B., Louisos, W., Hitt D.L., "Numerical Simulations Of Multiphase Flow In Supersonic Micro-Nozzles" 49th Aerospace Sciences Meeting Including the New Horizons Forum and Aerospace Exposition Orlando, Florida, 4-7 January 2011, *AIAA 2011-0189*

[10] Heister, S.D., Aderson, W.E. and Corpening, J.H., "A Model for Thermal Decomposition of Hydrogen Peroxide", 40th AIAA/ASME/SAE/ASEE Joint Propulsion Conference and Exhibit, Ft. Lauderdale, Florida, 11-14 July, 2004, *AIAA-2004-3373*

[11] Hitt, D.L., Zakrzwski, C. and Thomas, M., "MEMS-Based Satellite Micropropulsion Via Catalyzed Hydrogen Peroxide Decomposition", J. Smart Material & Structures, Volume 10, pp. 1163-1175, 2001

[12] Incropera, F., DeWitt, D., Bergman, T. and Lavine, A., "Funfementals of Heat and Mass Transfer," 6yh Ed, John Wiley & Sons, 2007.

[13] S. Janson, The History of Small Satellites, In H. Helvajian and S. Janson (Eds.). Small Satellites: Past, Present and Future. (pp. 45-87). El Segundo, CA, 2008.

[14] Louisos, W.F. and Hitt, D.L., "Viscous Effects on Performance of Two-Dimensional Supersonic Linear Micronozzles AIAA Journal of Spacecraft & Rockets, Vol. 45, No. 4, 2008.

[15] Maricelti, N., "Numerical simulations of hydrogen peroxide decomposition in a monolithic catalyst for rocket engines applications", Seventh Pegasus - AIAA Student Conference, Tornino, Italy, April, 28, 2011. t

[16] McCormick, J."Hydrogen Peroxide Rocket Manual" FMC Corporation, Pasadena, Texas, 1965.

[17] McDevitt, M. and Hitt, D. "Numerical Study of Disperse Monopropellant Slug Formation at a Cross Junction," Proceedings of the 41st AIAA Fluid Dynamics Conference, AIAA, Honolulu, Hawaii, June 2011.

[18] McDevitt, M. "Numerical Study of Disperse Monopropellant Microslug Formation at a Cross Junction," MS Thesis, University of Vermont, 2011.

[19] Mueller, J.,"Thruster Options for Microspacecraft: a review and valuation of the state-of-the art and emerging technologies", in Micropropulsion for Small Spacecraft - Progress in Astronautics and Aeronautics, M. Micci and A. Ketsdever, eds., vol. 187, AIAA, Reston, Va., p. 45-137, 2000.

[20] Orr, J.R. and Williams H.L., "Kinetics of the Reactions Between Iron (II) and some Hydroperoxides Based upon Cumene and Cyclohexane", J. Phys. Chem, Vol. 57, pp. 925-931, 1953.

[21] Rusek, J.J., "New Decomposition Catalysts and Characterization Techniques for Rocket-Grade Hydrogen Peroxide", Journal of Propulsion and Power, Vol. 12, No. 3, pp. 574-579, 1996.

[22] Sellers, J., Brown R. and Paul, M., "Practical Experience with Hydrogen Peroxide Catalysts", Proceedings of the 1st Annual Hydrogen Peroxide Conference, Surrey, United Kingdom, 1998.

[23] Thomas, A.,"Design and Testing of a Hydrogen Peroxide Microelectricalmechanical System", Ph.D thesis George Washington University, 2000.

[24] Whitehead, J."Hydrogen Peroxide Propulsion for Smaller Satellites", 1st International Hydrogen Peroxide Propulsion Conference, University of Surry, UK, 1998.

[25] Zhou, X. and Hitt, D.L., "One-Dimensional Modeling of Catalyzed H_2O_2 Decomposition in Microchannel Flows", 33rd AIAA Fluid Dynamics Conference and Exhibit, Orlando, Florida, 23-26 June, 2003, *AIAA-2003-3584*

[26] Zhou, X. and Hitt, D.L., "Modeling of Catalyed Hydrogen Peroxide Decomposition in Slender Microchannels with Arrhenius Kinetics", 40th AIAA/ASME/SAE/ASEE Joint Propulsion Conference and Exhibit, Ft. Lauderdale, Florida, 11-14 July, 2004, *AIAA-2004-3763*

[27] Zhou, X. and Hitt, D.L. , "Numerical Modeling of Monopropellant Decomposition in a Micro-Catalyst Bed', 35rd AIAA Fluid Dynamics Conference and Exhibit, Toronto, Canada, 6-9 June, 2005, *AIAA-2005-5033*

Appendix A

A.1 Certification of Analysis

A.2 FMC 50% to 91% H2O2 Sample Checklist

A.3 Standard Operating Procedure

FMC

Bayport Texas
90% HTP

CERTIFICATE OF ANALYSIS

Ship to: UNIVERSITY OF VERMONT
33 COLCHESTER AVE, 122A VOTEY BUILD
BURLINGTON VT 05405

Product: Hydrogen Peroxide 90% HTP
Batch #: A74203032010
Ship Date: 06-30-2010

Properties	Limits	Results	Units
Hydrogen Peroxide	90.0 - 91.5	90.8	%Wt.
Stability, 24 hr	98.0% min	99.6	
Total Carbon (C)	40 max	9	ppm
Ammonium (NH_4^+)	3.0 max	1.4	ppm
Evaporated Residue	20 max	4	ppm
Chloride (Cl)	0.50 max	0.05	ppm
Sulfate (SO_4)	0.50 max	0.12	ppm
Phosphate (PO_4)	0.20 max	0.08	ppm
Nitrate (NO_3)	5.0 max	4.0	ppm
Tin (Sn)	1.0 – 4.0 max	1.9	ppm
Antimony (Sb)	0.03 max	<0.01	ppm
Gold (Au)	0.03 max	<0.01	ppm
Titanium (Ti)	0.03 max	<0.01	ppm
Zinc (Zn)	0.03 max	0.01	ppm
Arsenic (As)	0.03 max	<0.01	ppm
Lead (Pb)	0.03 max	<0.01	ppm
Aluminum (Al)	0.35 max	0.02	ppm
Chromium (Cr)	0.03 max	0.01	ppm
Manganese (Mn)	0.03 max	<0.01	ppm
Iron (Fe)	0.03 max	0.01	ppm
Nickel (Ni)	0.03 max	0.01	ppm
Copper (Cu)	0.03 max	<0.01	ppm

Authorization Signature

FMC 52% to 91% H2O2 Sample Checklist

Customer: Stephen Widdis **Location:** University of Vermont
Customer Contact: 33 Colchester Ave, Burlington Vt 05401 **Phone Number:** 732-859-4552
Application: Rocket Fuel
H2O2 %: 90 **H2O2 Grade:** HTC

52% to 91% Hydrogen Peroxide

	System Requirement	Yes/No
1.	Any new or significantly modified hydrogen peroxide (H_2O_2) storage facility has been reviewed and approved by the local authority having jurisdiction (e.g. Fire Marshal, Building Inspector, etc.). If >200 pounds stored written notification has been provided to the local authority having jurisdiction.	Yes
2.	The LEPC, SERC and fire department has/will be provided a MSDS if storing ≥500 pounds of H2O2 per 40 CFR 370. **Note: Must also include on next annual report.**	N/A
3.	The H_2O_2 storage facility has appropriate security measures are in place.	Yes
4.	The H_2O_2 storage facility has a suitable emergency plan in place.	Yes
5.	Personnel involved in the handling of H_2O_2 have received appropriate H_2O_2 safety training	Yes
6.	A clean water source is readily available where H_2O_2 is stored; additionally, a safety shower/eye wash station is available wherever H_2O_2 is used.	Yes
7.	>52% H_2O_2 storage areas are conspicuously identified by the words "Class 3 Oxidizers."	Yes
8.	Smoking is prohibited in all H_2O_2 storage areas; "No Smoking" signs are conspicuously posted.	Yes
9.	H_2O_2 samples are stored away from heat sources, combustibles and incompatible chemicals such as other oxidizing agents, reducing agents, caustic etc.; and are recommended to be stored out of direct sunlight.	Yes
10.	H_2O_2 samples are stored in upright position at all times, and sample bottle cap breather vent is not blocked.	Yes
11.	Ambient temperature of >52% H_2O_2 storage area does not exceed 40°C (104°F).	Yes
12.	H_2O_2 storage areas are well ventilated.	Yes
13.	H_2O_2 storage area is provided with adequate secondary containment.	Yes
14.	All H_2O_2 "wetted" equipment is compatible with H_2O_2, and is dedicated for H_2O_2 use only. **Note: PE, PP, PVC or any other plastic components (i.e. with the exception of Teflon or Teflon derivatives) are not approved for use in >52% H_2O_2 service.**	Yes
15.	Any "wetted" H_2O_2 components have been properly passivated for H_2O_2 service.	Yes
16.	Equipment used for dispensing/transferring H_2O_2 from the samples is thoroughly flushed with clean water and properly secured (i.e. to prevent introduction of contaminants) before and after each use.	Yes
17.	All H_2O_2 transfer systems are designed to avoid areas where peroxide can be trapped. Design ensures that any pressure/gas generated can be safely released. All H_2O_2 valves are properly vented.	N/A
18.	H_2O_2 transfer systems are designed to prevent back flow of process or water streams into the H_2O_2 drum.	N/A
19.	>52% H_2O_2 transfer systems are completely drained and/or purged with clean water or nitrogen after each use.	N/A
20.	H_2O_2 samples should not be transferred to other containers for shipping without checking with FMC on approved containers and methods for shipping.	N/A

Stephen Widdis — **Form Completed by**

6/08/2010 — **Date**

Comments (note number of deficiency):

STANDARD OPERATING PROCEDURE
90% HYDROGEN PEROXIDE SOLUTION

Principal Investigator: Darren Hitt **Phone number: _____**

Room & Building: Votey 122A

Emergency Contact Information: Stephen Widdis (732) 859-4552

I have read and understand the SOP:

Name: **Signature:** **Date:**

---

1. INFORMATION ABOUT 90% HYDROGEN PEROXIDE AND PROCEDURES USING 90% HYDROGEN PEROXIDE

CAS# 7722-84-9
90% Hydrogen Peroxide is a clear, colorless liquid that is classified as a strong oxidizer and a corrosive liquid. It is commonly used as a laboratory reagent and in this case will be rapidly decomposed using a verity of catalysts to produce thrust.

2. HAZARDOUS PROPERTIES, POTENTIAL ROUTES OF EXPOSURE, SYMPTOMS OF EXPOSURE

90% Hydrogen peroxide is an irritant of the eyes, mucous membranes, and skin.

Routes of Exposure
Skin or eye contact, ingestion or inhalation of the vapor or mist.

Acute Effects:
The signs and symptoms of acute exposure to hydrogen peroxide include irritation of the eyes, nose, throat and lungs, ranging from mild bronchitis to pulmonary edema. Liquid or spray mist may produce tissue damage particularly on mucous membranes of eyes, mouth and respiratory tract. Skin contact may produce burns. Inhalation of the spray mist may produce severe irritation of respiratory tract, characterized by coughing, choking, or shortness of breath. Corneal ulceration, redness and blisters on the skin, and bleaching of hair might occur after contact of the eyes or skin with the liquid or vapor. Ingestion of large doses may cause symptoms of abdominal pain, vomiting, and diarrhea as well as blistering or tissue destruction. Stomach distention (due to rapid liberation of oxygen), and risk of stomach perforation, convulsions, pulmonary edema, coma, possible cerebral edema (fluid on the brain), and death are possible.

Chronic Effects:
No signs or symptoms of chronic exposure to hydrogen peroxide have been reported in humans.

Exposure Limits:
The current OSHA permissible exposure limit (PEL) for hydrogen peroxide is 1 ppm (1.4 mg/m^3) as an 8-hour time-weighted average (TWA) concentration. The NIOSH recommended exposure limits (RELs) for hydrogen peroxide is 1 ppm (1.4 mg/m^3) as a TWA for up to a 10-hour workday and a 40-hour workweek. The American Conference of Governmental Industrial Hygienists (ACGIH) assigned hydrogen peroxide a threshold limit value (TLV) of 1 ppm (1.4 mg/m^3) as a TWA for a normal 8-hour workday and a 40-hour workweek. The NIOSH limit is based on the risk of eye, mucous membrane and skin irritation. The ACGIH limit is based on the risk of irritation.

3. PERSONAL PROTECTIVE EQUIPMENT

- Use of nitrile, PVC, neoprene or Viton gloves is recommended when handling hydrogen peroxide.
- Safety glasses with side shields, face shield, or chemical splash goggles shall be worn.
- A flame-retardant coat should be worn when working with hydrogen peroxide.
- Closed toe shoes are required when working in the laboratory.
- Do not wear or use cotton, wool or leather, as these materials react RAPIDLY with higher concentrations of hydrogen peroxide.

4. ENGINEERING/VENTELAVTION CONTROLS

- Safety shower and eye wash stations should be easily accessible where 90% hydrogen peroxide is used. Note: The closest safety shower and eyewash unit is near Floyd's office in the 122B area. Take a turn at activating both before using this chemical.
- A clean beaker containing 100 ml of distilled water for every 1 ml of hydrogen peroxide being used shall be present on the laboratory bench.
- The path to the laboratory sink shall not be blocked or obstructed in anyway will experiments with hydrogen peroxide are being conducted.
- Fume hoods should be used when using large quantities and when potential for reaction releasing hazardous products exists.

5. SPECIAL HANDLING PROCEDURES AND STORAGE REQUIREMENTS

- Store 90% hydrogen peroxide in a cool, dark, dry, well-ventilated area **in a vented container**. Votey 122A has a flammable cabinet that is vented by loosening the flash arrestors on the side of the cabinet and is used to store 90% hydrogen peroxide only. Do not store any other chemicals in this cabinet. The cabinet is marked with an "Oxidizer" label.
- Containers of hydrogen peroxide should be protected from physical damage. Glass, polyethylene, stainless steel and aluminum are recommended materials for storage containers.
- Store separately from combustible materials such as wood, paper, oil, etc., organic materials such as alcohols, acetone, and other ketones; Aldehydes, and their anhydrides; glycerol, cotton (cellulose), metals including iron, copper, chromium, lead, silver, manganese, sodium, potassium, magnesium, nickel, gold, platinum; metal alloys such as brass or bronze; metal oxides such as lead oxides, mercury oxides, or manganese dioxide; and many metal salts, like potassium permanganate or sodium iodate. Tremendous explosion can be caused by unstable mixtures with concentrated mineral acids.
- Wash hands thoroughly after handling hydrogen peroxide (even if gloves were used).
- Remove contaminated clothing/PPE and wash before reuse.
- Transport chemicals in closed containers, in the smallest amounts possible.
- It is highly recommended that all chemicals be stored below eye level so cracking or leaking containers are immediately visible and there is less potential for chemicals falling onto lab workers when pulling from shelves. Inspect chemical containers regularly.

6. PROCEDURE USING 90% Hydrogen Peroxide

- **Preparatory Work**
  - Fill ultrasonic bath with de-ionized water and detergent mixture.
  - Rinse glassware with tap water.
  - Rinse glassware with de-ionized water.
  - Place glassware in bath and run for 30 minutes with heat.
  - Rinse glassware with de-ionized water.
  - Place in oven at 120° C until dry
  - Allow to cool in oven
- **Handling 90% Hydrogen Peroxide**
  - Wear appropriate PPE (nitrile gloves, safety glasses with side shields or face shields, flammable resistant lab coat).
  - Work in a well-ventilated area.
  - Change nitrile gloves after handling 90% Hydrogen Peroxide. Rinse nitrile gloves with water before disposing in trash. (let's talk about this to be more specific)
  - Place 100 ml of distilled water for ever 1 ml of H202 that will be used in open container on bench top
  - Unlock and open flammables cabinet
  - Remove 90% hydrogen peroxide bottle and the secondary containment
  - Over secondary containment, pour needed quantity from primary containment into appropriate size glass beaker.
- **Experimental Procedure**
  - Make 3 ml of 35% H_2O_2 by adding 1 ml of H_2O_2 to 2 ml of water
  - Fill syringe (glass or plastic) with 35% H_2O_2 and run through teflon or stainless tubing
    - Observe for evaporation or increased temperature (is there a thermometer? How would one note the temp change). If any is observed, than a contaminant is present and the material has not been properly conditioned. Flush with de-ionized water and repeat steps. Collect waste in a glass container. Be sure to dilute all waste to less than 3% H_2O_2 by volume
    - If no heat generation is observed, the test setup has been properly conditioned and the experiment may proceed.
  - Create another mixture of desired concentration.
  - Place clean syringe tip in H_2O_2 and withdrawal needed amount. Never re-use a syringe without thorough cleaning. Always use a new one in virgin H202 container?
  - Connect syringe to system with lure type connection and perform experiment
  - Collect all remaining hydrogen peroxide in a glass beaker and follow UVM waste disposal procedure.

7. SPILL AND ACCIDENT PROCEDURES

- Water dilution is the primary way to cleanup spilled 90% hydrogen peroxide. However, do not attempt cleanup if you feel unsure of your ability to do so or if you perceive the risk to be greater than normal laboratory operators.
- In the event of skin contact, immediately wash with mild soap and copious amounts of water and seek medical attention. Remove contaminated clothing and shoes. Completely submerge hydrogen peroxide contaminated clothing in water prior to drying; if allowed to dry on clothing, evaporation leads to concentration and increased possibility of ignition.
- In case of contact with eyes, immediately flush eyes with copious amounts of water with emergency eyewash in the hallway for at least 15 minutes (lifting upper and lower eyelids occasionally) and obtain medical attention. You may need assistance to flush your eyes properly.
- If inhaled, move to fresh air immediately and seek medical attention. If victim is not breathing, perform CPR.
- In the event of ingestion, obtain medical attention immediately. Do not induce vomiting. Give the victim large quantities of water to drink. Never give anything by mouth to an unconscious person. Loosen tight clothing such as a collar, tie, belt or waistband. Keep victim warm and quiet until medical help arrives.

- Note to Physician: Pulmonary edema may be delayed for 24-72 hours; keep under observation. Gastic lavage may be necessary if swallowed. Analysis of body fluids (particularly gastric aspirates) using the titanium chloride reaction, if done immediately, will reveal peroxides.

Small spills:

Don nitrile gloves, face shield, and flame-retardant lab coat.. Remove all sources of heat and ignition; keep combustibles (wood, paper, oil etc) away from spilled material. Evacuate all unprotected personnel and ventilate area. Absorb with spill pad from Chemical Spill Kit or flood the area with large amounts of water. Dilute to less than 5% by volume and clean with absorbent pad in lab chemical spill kit.

Large spills:

Notify others in room of spill by placing the "spill in progress" signage that is in the chemical spill kit on the lab outer door. Evacuate room/immediate area. Call 656-2560, press 1 and request that they page UVM Environmental Safety. If large spill, leave the area and call 9-1-1. Keep away from heat or sources or ignition. Stop leak if without risk. Flood the area with large amounts of water and dike far ahead of the spill to contain the hydrogen peroxide for later reclamation and disposal. Post warning signs at entrances/exits notifying others of spill. Prevent unnecessary entry into area. Provide assistance and information to spill responders.

8. WASTE DISPOSAL PROCEDURES

- **For quantities less than 25 ml**
  - Dilute to less than 3% by volume
  - Pour down drain.
- 90% Hydrogen Peroxide Aqueous Solution is classified as a 5.1 oxidizer and 8A Corrosive Liquid. **Hydrogen Peroxide waste and solutions should be properly disposed of through UVM ESF.**

9. MSDS LOCATION

Material Safety Data Sheet is located in MSDS binder affixed to the wall just inside the laboratory door.

References: Information contained in this SOP was gathered from the following sources: JT Baker MSDS, OSHA (http://www.osha.gov/SLTC/healthguidelines/hydrogenperoxide/recognition.html), Science Lab.com MSDS.